

Biological Regulation of Atmospheric Chemistry En Route to Planetary Oxygenation

Shortened Working Title: Biogenic Haze Formation Fuels Planetary Oxidation

Classification: Physical Sciences: Earth, Atmospheric, and Planetary Sciences.

Authors^{affiliations}, **Email Addresses [ORCID ID]:**

Gareth Izon^{a,1,2}, Garethjizon@googlemail.com; gizon@MIT.edu [0000-0003-2742-4922]

Aubrey L. Zerkle^a, az29@st-andrews.ac.uk [0000-0003-2324-1619]

Kenneth H. Williford^b, kenneth.h.williford@jpl.nasa.gov [0000-0003-0633-408X]

James Farquhar^c, jfarquha@umd.edu

Simon W. Poulton^d, s.poulton@leeds.ac.uk

Mark W. Claire^{a,e}, mc229@st-andrews.ac.uk [0000-0001-9518-089X]

Affiliation and Correspondence Footnotes:

^a School of Earth and Environmental Sciences, Centre for Exoplanet Science, University of St Andrews, St Andrews KY16 9AL, Scotland, UK.

^b Jet Propulsion Laboratory, California Institute of Technology, 4800 Oak Grove Drive, Pasadena, CA 91109, United States of America.

^c Department of Geology and Earth System Science Interdisciplinary Center, University of Maryland, College Park, MD 20742, United States of America.

^d School of Earth and Environment, University of Leeds, Leeds LS2 9JT, United Kingdom.

^e Blue Marble Space Institute of Science, 1001 4th Ave, Suite 3201, Seattle, WA 98154, USA.

¹Present Address: Department of Earth, Atmospheric and Planetary Sciences, Massachusetts Institute of Technology, Cambridge, MA 02139.

²Correspondence to be addressed to Gareth Izon: garethjizon@googlemail.com | gizon@MIT.edu

Contributions: GI and AZ conceived the project. GI, AZ, MC and SP collected the samples. GI and KW analyzed samples. MC developed the photochemical models and ran the simulations. GI interpreted the data and wrote the manuscript with input from all co-authors. The authors declare no competing financial interests.

Key Words: Sulfur Mass Independent Fractionation | Neoproterozoic | Organic Haze | Hydrogen Loss | Planetary Oxidation

Accepted for publication in *Proceedings of the National Academy of Sciences* on 3rd February, 2017

ABSTRACT: Emerging evidence suggests that atmospheric oxygen may have varied before rising irreversibly ~2.4 billion-years-ago, at a time when primary atmospheric proxies indicate reducing conditions. Significantly, however, temporal atmospheric aberrations towards more reducing conditions—featuring a methane-derived organic-haze—have recently been suggested, although their occurrence, causes and significance remain under-explored. To examine the potential role for haze formation in Earth’s history, we targeted an episode of inferred haze development. Our redox controlled (Fe-speciation) carbon- and sulfur-isotope record reveals sustained systematic stratigraphic covariance, precluding alternate, non-atmospheric, explanations. New photochemical models corroborate this inference, showing $\Delta^{36}\text{S}/\Delta^{33}\text{S}$ ratios are sensitive to the presence of haze. Utilizing existing age constraints, we estimate that organic-haze developed rapidly, stabilizing within $\sim 0.3 \pm 0.1$ Myr, and persisted for upwards of $\sim 1.4 \pm 0.4$ Myr. Given these temporal constraints and the elevated atmospheric $p\text{CO}_2$ in the Archean, the sustained methane fluxes necessary for haze formation can only be reconciled with a biological source. Correlative $\delta^{13}\text{C}$ and TOC measurements support the interpretation that atmospheric haze was a transient response of the biosphere to increased nutrient availability, with net methane fluxes controlled by the relative availability of organic-carbon and sulfate. Elevated $p\text{CH}_4$ during haze episodes would have expedited planetary hydrogen loss, with a single episode of haze development providing up to $2.6\text{--}18 \times 10^{18}$ moles of O_2 equivalents to the Earth system. Our findings suggest the Neoproterozoic likely represented a unique state of the Earth System where haze development played a pivotal role in planetary oxidation hastening the contingent biological innovations that followed.

SIGNIFICANCE STATEMENT: It has been proposed that enhanced methane fluxes to Earth’s early atmosphere could have altered atmospheric chemistry, initiating a hydrocarbon-rich haze reminiscent of Saturn’s moon, Titan. The occurrence, cause and significance of haze development, however, remain unknown. Here, we test and refine the “haze hypothesis” by combining an ultra-high-resolution sulfur- and carbon-isotope dataset with photochemical simulations to reveal the structure and timing of haze development. These data suggest that haze persisted for ~ 1 Myr, requiring a sustained biological driver. We propose that enhanced atmospheric CH_4 , implied by the presence of haze, could have had a significant impact on the escape of hydrogen from the atmosphere, effectively contributing to the terminal oxidation of Earth’s surficial environments at ~ 2.4 Ga.

\body

INTRODUCTION

Quadruple sulfur isotope fractionation is one of the most robust geochemical tools available to constrain the atmosphere's redox state, owing to intrinsic links between atmospheric photochemistry and oxygen (1-11). Prior to ~2.4 Ga (5, 6), sedimentary S-phases display mass independent S-isotope fractionation (S-MIF; $\Delta^{33}\text{S}$ and $\Delta^{36}\text{S} \neq 0^1$), which is conspicuously absent in the younger geological record (5-7, 11). The disappearance of S-MIF is widely cited as reflecting a critical change in atmospheric state, where oxygen exceeded 0.001% of present atmospheric levels (3) during the so-called Great Oxidation Event (GOE; 4, 5, 6, 12). More recently, however, the perception of the GOE *sensu stricto* has been questioned by emerging data derived from 3.0–2.5 Ga sediments, interpreted to represent both earlier accumulation(s) of atmospheric oxygen/ozone (13-16), as well as transient descents toward a reduced methane-rich atmospheric state (8, 9, 17, 18).

Interrogation of the temporal S-MIF record reveals additional details—variable magnitude and changes in $\Delta^{36}\text{S}/\Delta^{33}\text{S}$ slope—which are suggested to reflect subtle atmospheric compositional changes beyond the simple presence or absence of oxygen (6-10, 12, 17, 19-21). Specifically, geochemical records from multiple continents reveal a broad correlation between changes in the S-MIF record and highly ^{13}C -depleted organic carbon—termed C-S anomalies (8)—which have been interpreted to reflect the periodic formation of a hydrocarbon haze reminiscent to that observed on Saturn's moon Titan (8-10). While these records have been used to paint an intriguing picture of Neoproterozoic atmospheric dynamics in the prelude to the GOE (8, 9), a critical appraisal of the Neoproterozoic haze hypothesis awaits (22). We present new, high-resolution, coupled quadruple sulfur- and carbon-isotope, Fe-speciation, and TOC records (Figure 1) from the youngest of the three C-S anomalies identified in core GKF01, obtained from Griqualand West Basin, South Africa (SI Appendix, Figure 1A; SI Appendix; 9, 15, 23, 24), resulting in the highest temporal-resolution stratigraphic study yet conducted in the Archean. Critical to testing the haze hypothesis, our geochemical records reveal the timing and structure of a C-S anomaly, which when combined with an updated photochemical model, demonstrate a connection between changes in $\Delta^{36}\text{S}/\Delta^{33}\text{S}$ slope and

¹ Sulfur-isotope ratios are conventionally reported in delta (δ) notation, and reflect the permil (‰) deviation of the ratio of the least abundant ($^{33}\text{S}, ^{34}\text{S}, ^{36}\text{S}$) to the most isotope (^{32}S) relative to the same ratio in an international reference standard (Vienna Canyon Diablo Troilite, V-CDT). For example, $\delta^{34}\text{S} = ((^{34}\text{S}/^{32}\text{S})_{\text{sample}} / (^{34}\text{S}/^{32}\text{S})_{\text{V-CDT}}) - 1$. The majority of processes fractionate S-isotopes mass dependently, whereby $\delta^{33}\text{S} \approx 0.515 * \delta^{34}\text{S}$ and $\delta^{36}\text{S} \approx 1.91 * \delta^{34}\text{S}$. Departure from mass-dependent behavior, or mass-independent fractionation (MIF), is expressed in capital-delta (Δ) notation as either non-zero $\Delta^{33}\text{S} [(^{33}\text{S}/^{32}\text{S})_{\text{sample}} / (^{33}\text{S}/^{32}\text{S})_{\text{V-CDT}} - ((^{34}\text{S}/^{32}\text{S})_{\text{sample}} / (^{34}\text{S}/^{32}\text{S})_{\text{V-CDT}})^{0.515}]$ or $\Delta^{36}\text{S} [(^{36}\text{S}/^{32}\text{S})_{\text{sample}} / (^{36}\text{S}/^{32}\text{S})_{\text{V-CDT}} - ((^{34}\text{S}/^{32}\text{S})_{\text{sample}} / (^{34}\text{S}/^{32}\text{S})_{\text{V-CDT}})^{1.9}]$.

atmospheric haze. Following this, we speculate on the wider role of episodic haze formation in planetary oxidation.

RESULTS

In core GKF01, the upper Nauga Formation reveals large multiple S-isotope variability, with non-zero $\Delta^{33}\text{S}$ and $\Delta^{36}\text{S}$ (Figures 1–2, SI Appendix, Fig. S2) reflecting photochemical production in an atmosphere devoid of significant oxygen (1-3, 6, 7). The majority of these data form a linear $\Delta^{36}\text{S}/\Delta^{33}\text{S}$ array (Figure 2), typifying core GKF01 (9, 18) and the wider Neoproterozoic as a whole ($\Delta^{36}\text{S} \approx -0.9 \times \Delta^{33}\text{S}$). Of importance for this study, the $\Delta^{36}\text{S}/\Delta^{33}\text{S}$ record reveals a coherent stratigraphic structure, with a remarkably stable background ($\Delta^{36}\text{S}/\Delta^{33}\text{S} = -0.9$) punctuated by a spectacular negative excursion between 840.0 and 827.87 m core depth. During the excursion $\Delta^{36}\text{S}/\Delta^{33}\text{S}$ ratios become increasingly negative (Figure 1B), attaining a steeper slope of ~ -1.5 , before relaxing back towards the background $\Delta^{36}\text{S}/\Delta^{33}\text{S}$ (-0.9 ; Figures 1–2). While the $\Delta^{36}\text{S}/\Delta^{33}\text{S}$ data displays little variability outside of the identified excursion (Figure 2), the magnitude of the $\Delta^{33}\text{S}$ and $\Delta^{36}\text{S}$ is highly variable, carrying positive and negative arithmetic signs, respectively (SI Appendix, Fig. S2). Consequently, it appears that the dominant sulfur source for pyrite formation over the examined interval was elemental sulfur, inferred to carry a positive $\Delta^{33}\text{S}$ (7, 18, 25). Atypically, the $\delta^{34}\text{S}$ record displays little variability, with the exception of two relatively more ^{34}S depleted samples seen at ~ 840 m (Figure 1).

Moving in phase, or perhaps even leading the S-isotope record, $\delta^{13}\text{C}_{\text{Org}}$ is also observed to descend to extremely low values (less than -37 ‰; Figure 1b); a relationship that is particularly apparent in Figure 3a where $\Delta^{36}\text{S}/\Delta^{33}\text{S}$ less than -1 corresponds to $\delta^{13}\text{C}_{\text{Org}}$ ² less than -37 ‰, and the most ^{13}C -depleted samples relate to the lowest $\Delta^{36}\text{S}/\Delta^{33}\text{S}$. We observe additional low $\delta^{13}\text{C}_{\text{Org}}$ values (~ -35 ‰) below the C-S anomaly that are not associated with changes in $\Delta^{36}\text{S}/\Delta^{33}\text{S}$, but correspond to small-scale increases in TOC typical of the intercalated mudstones that are below the scale to be represented in Figure 1.

The C-S anomaly is not confined wholly to the mudstone interval, as cursory consideration of Figure 1 would suggest. The decreases in both geochemical parameters are observed to have occurred by 840 m core depth; however, close inspection of detailed core logs/photos (SI Appendix, Fig. S3) shows that a lithological change from carbonate to mudstone occurs 0.6–1.0 m above this horizon. Similarly, while the most depleted $\Delta^{36}\text{S}/\Delta^{33}\text{S}$ ratios are confined to the basal-half of the mudstone, the return to background $\Delta^{36}\text{S}/\Delta^{33}\text{S}$ is not established until

² Carbon-isotope data are expressed as permil deviations from the Vienna-PeeDee Belemnite (V-PDB) standard: $\delta^{13}\text{C}_{\text{Org}} = ((^{13}\text{C}/^{12}\text{C}_{\text{Sample}})/(^{13}\text{C}/^{12}\text{C}_{\text{V-PDB}})) - 1$.

827.8 m, some 1.5m above the reestablishment of calcareous sedimentation (Figures 1; SI Appendix, Fig. S3). These observations require chemostratigraphic controls beyond simple facies or lithological changes.

DISCUSSION

THE CAUSES AND SIGNIFICANCE OF THE SULFUR AND CARBON ISOTOPE COVARIATION

The broad correspondence between low $\Delta^{36}\text{S}/\Delta^{33}\text{S}$ and $\delta^{13}\text{C}_{\text{Org}}$ has formed the cornerstone of the “haze hypothesis”, whereby enhanced methane flux (manifested as low $\delta^{13}\text{C}_{\text{Org}}$) is hypothesized to have promoted organic-haze formation and altered atmospheric chemistry (registered as $\Delta^{36}\text{S}/\Delta^{33}\text{S}$; 8, 9). The low-resolution records generated in these prior studies, however, have precluded rigorous examination of this hypothesized link, which in turn has obfuscated the wider role of haze formation within the evolution of the ancient Earth system. As a result this early work failed to reveal the stratigraphic structure of a C-S anomaly beyond a few scattered data points. Our geochemical records (Figures 1; SI Appendix, Fig. S2) provide a framework from which to examine the origin of the observed C- and S-isotope covariation.

The $\delta^{13}\text{C}$ of sedimentary organic matter is an integrated product, combining varying contributions from different biological sources. Contemporary and Phanerozoic $\delta^{13}\text{C}_{\text{Org}}$ records display restricted variability owing to the limited C-isotope fractionation associated with heterotopic respiration. The Neoproterozoic, by contrast, features a more pronounced range of $\delta^{13}\text{C}_{\text{Org}}$, indicating more pervasive incorporation of ^{13}C -depleted substrates, particularly methane (26). Accordingly, the low $\delta^{13}\text{C}_{\text{Org}}$ ($< -37\text{‰}$) seen in the C-S anomaly, and probably the intermediate $\delta^{13}\text{C}_{\text{Org}}$ ($< -35\text{‰}$) in the basal part of the examined succession ($< 840\text{ m}$; Figure 1), speak to substantial methane incorporation into sedimentary organic matter. In greater detail, this incorporation involves the interplay between localized methane production (methanogenesis), oxidation and assimilation (methanotrophy; 26). Therefore, the low $\delta^{13}\text{C}_{\text{Org}}$ data observed in GKF01 (and other Neoproterozoic sedimentary successions) can be explained in two ways: (i) increased methanotrophy assimilating more methane into the sedimentary record independent of the methane flux (26, 27) or (ii) enhanced methanogenesis, increasing environmental methane availability, with a parallel increase in methanotrophy (8, 9). Sedimentary $\delta^{13}\text{C}_{\text{Org}}$ values are controlled *locally*, and reflect the carbon utilization strategies of the microbial communities from which the organic matter is sourced. Therefore, the haze hypothesis does not require every inflection in the $\delta^{13}\text{C}_{\text{Org}}$ record to correspond to altered atmospheric chemistry. In fact, one prediction of the haze hypothesis is that there should be instances where $\Delta^{36}\text{S}/\Delta^{33}\text{S}$ and $\delta^{13}\text{C}_{\text{Org}}$ are decoupled (8), such as below 840 m in core GKF01 (Figure 1).

AN ALTERNATE, NON-ATMOSPHERIC, CONTROL ON $\Delta^{36}\text{S}/\Delta^{33}\text{S}$?

The haze hypothesis is reliant on the $\Delta^{36}\text{S}/\Delta^{33}\text{S}$ parameter faithfully recording what is inferred to be regional to global-scale atmospheric chemistry. The high-resolution dataset we present here (Figure 1) provides the perfect opportunity to test alternative hypotheses, whereby non-atmospheric, sediment-hosted, processes could produce the observed changes in the $\Delta^{36}\text{S}/\Delta^{33}\text{S}$ record.

Biological metabolic processes are known to impart small mass-dependent effects during inter- and intra-cellular (un)mixing processes (19, 28). Biologically mediated mass conservation effects are known to preferentially effect $\Delta^{36}\text{S}$, resulting in distinctive $\Delta^{36}\text{S}/\Delta^{33}\text{S}$ slopes (~ 7 ; 28), potentially overprinting the atmospheric $\Delta^{36}\text{S}/\Delta^{33}\text{S}$ signal. The extent of such a biological overprint is quasi-predictably governed by initial source of pyrite-sulfur, producing a scalene mixing-field in $\Delta^{36}\text{S}-\Delta^{33}\text{S}$ quadruple-isotope space (Figure 2B; 29). Since microbial sulfate reduction (MSR) imparts the largest biological S-isotope fractionations, this biological effect is most pronounced when the pyrite-sulfur is dominated by a sulfate precursor (negative $\Delta^{33}\text{S}$) and becomes progressively more muted when elemental sulfur (positive $\Delta^{33}\text{S}$) dominates the pyrite-sulfur pool (29). Examination of Figures 2 and Fig. S2 (SI Appendix) reveals the pyrite throughout the studied interval carries a pronounced and exclusively positive $\Delta^{33}\text{S}$, in-turn implying an elemental sulfur source, which is expected to be less susceptible to modification by MSR (Figure 2). In addition to altering $\Delta^{33}\text{S}$ and $\Delta^{36}\text{S}$, microbial processes are also generally associated with pronounced changes in $\delta^{34}\text{S}$ (60–70‰; 30). However, as described above, the $\delta^{34}\text{S}$ record in the succession we examined is remarkably stable (Figures 1, 3C), offering little support for a biologically mediated model (19).

Thermochemical sulfate reduction (TSR) can also impart a distinctive S-MIF signature (Figure 2B); however, this process also cannot explain our S-isotope observations. Firstly, we see no evidence for selective hydrothermal activity associated with TSR in strata between 840.0 and 827.87 m. Decisively, TSR has been shown experimentally to impart large $\Delta^{33}\text{S}$ enrichments without significant changes in $\Delta^{36}\text{S}$ (31). Addition of TSR-derived sulfur, therefore, would serve to increase $\Delta^{36}\text{S}/\Delta^{33}\text{S}$ ratios, which is contrary to what we observe (Figure 2).

A final possibility invokes an additional, and isotopically distinct, S-MIF production pathway capable of producing an additional sulfur pool with a distinct and different $\Delta^{36}\text{S}/\Delta^{33}\text{S}$ (< -1.5), which could selectively contribute to pyrite genesis under variable conditions (32). The observed change in $\Delta^{36}\text{S}/\Delta^{33}\text{S}$ could, therefore, reflect electron donor availability, highlighting a potential localized control on the degree of pyritization, whereby high TOC permitted selective access to a recalcitrant sulfur pool. Following this scenario, the increased TOC

observed in the C-S anomaly (Figure 1), could potentially provide a sediment-hosted explanation for the observed coupled C- and S-isotope covariation. This explanation would require a ubiquitous association between low $\Delta^{36}\text{S}/\Delta^{33}\text{S}$, $\delta^{13}\text{C}_{\text{Org}}$ and high TOC, which is not observed in our data or in previous datasets (Figures 1–3; 8, 9, 22). For example, closer examination of Figure 3B shows there are samples that are enriched in TOC (~ 1 Wt. %) yet display typical $\Delta^{36}\text{S}/\Delta^{33}\text{S}$ ratios (-0.9). Similar trends are also obvious in published records, with typical $\Delta^{36}\text{S}/\Delta^{33}\text{S}$ ratios being frequently observed in tandem with high TOC abundances (5 % Wt. %; 9). Also, if sedimentary $\Delta^{36}\text{S}/\Delta^{33}\text{S}$ ratios were truly independent of time-dependent changes in atmospheric chemistry, the necessary refractory sulfur pool should be ever-present (independent of lithology) and should be observed in other portions of the geological record. For instance, a secondary sedimentary sulfur pool might be expected to be intermittently incorporated into pyrite under a particular range of depositional conditions, producing highly variable $\Delta^{36}\text{S}/\Delta^{33}\text{S}$ values. This is not the case here (Figure 1), and is also at odds with the wider Archean $\Delta^{36}\text{S}/\Delta^{33}\text{S}$ record (19). Moreover, SIMS analyses reveal that $\Delta^{36}\text{S}/\Delta^{33}\text{S}$ trends are conserved at the grain scale between different populations of pyrite within the GKF01 core as a whole (18). Therefore, any model driven by electron donor availability, reliant on a “ghost sulfur pool”, cannot be responsible for the observed change in $\Delta^{36}\text{S}/\Delta^{33}\text{S}$ revealed in the C-S anomaly (Figure 1). Taken together, sediment-hosted processes, such as biological modification, thermochemical alteration and differential pyrite genesis, fail to satisfactorily explain the systematic changes in $\Delta^{36}\text{S}/\Delta^{33}\text{S}$ starting at 840 m, leaving an atmospheric origin as the most parsimonious explanation of these data.

PHOTOCHEMICAL MODELING OF $\Delta^{36}\text{S}/\Delta^{33}\text{S}$

Assimilating the arguments above, the two isotopic systems (C and S) that form the keystone of the haze hypothesis are sensitive to perturbations on different spatial, and potentially temporal, scales. In principle, low $\delta^{13}\text{C}_{\text{Org}}$, and hence methane production/consumption, should be ubiquitous in the Archean, responding to local-scale changes in organic matter quality and quantity (8, 9, 26). In an atmospheric sense, however, it is unlikely that a short-lived change akin to what we observed in the intercalated subordinate mudstones in the basal part of the succession (> 840 m depth; Figure 1) would result in a change in atmospheric methane concentrations capable of instigating haze formation. Instead, it would require a sustained regional increase in methane fluxes, caused by changes in nutrient delivery or redistribution in the oceans (discussed below), to plausibly increase atmospheric $p\text{CH}_4$ sufficiently to instigate haze formation. If haze development was substantial enough to

enshroud the planet, it is also possible that $\Delta^{36}\text{S}/\Delta^{33}\text{S}$ could be decoupled from $\delta^{13}\text{C}_{\text{Org}}$, if the site of methane production/consumption was occurring elsewhere.

To examine the direct link between $\Delta^{36}\text{S}/\Delta^{33}\text{S}$ values and atmospheric chemistry, we updated an Archean 1-D photochemical model (7) to predict $\Delta^{33}\text{S}$, $\Delta^{36}\text{S}$, and trace $\Delta^{36}\text{S}/\Delta^{33}\text{S}$ ratios through an atmospheric reaction network. Details of the model and our preliminary validation approach are provided in the [SI Appendix](#). The most significant changes from the initial predictions of Claire et al. (7) arise from the inclusion of new data allowing $\Delta^{36}\text{S}$ predictions, and the use of newly measured SO_2 photodissociation cross-sections (33). As noted previously (7, 34), the earlier SO_2 cross-sections (35) produced results at odds to the commonly accepted interpretation of the geologic record: predicting positive $\Delta^{33}\text{S}$ in sulfate and negative $\Delta^{33}\text{S}$ in elemental sulfur. Incorporating the revised cross-sections (33) resolve this data-model mismatch, and now predict exit channels with the arithmetic sign commonly seen in the rock record ([Figures 4–5](#)). However, it is important to note our model still fails to reproduce both the magnitude of the S-MIF and the $\Delta^{36}\text{S}/\Delta^{33}\text{S}$ ratio archived in the geological record ([Figures 1, 4–5; S SI Appendix](#)). A detailed exploration of this discrepancy exceeds the scope of this study, but likely reflects uncertainties concerning the primary S-MIF generating mechanism(s) included within the model and/or the composition of the Archean background state ([Figure 4; 7](#)). Both of these potential sources of uncertainty are the focus of on-going research and remain fundamental to successful inverse reconstruction of the Archean atmosphere.

[Figure 4A](#) provides insight into the transmittance of $\Delta^{36}\text{S}/\Delta^{33}\text{S}$ ratios through an atmospheric reaction network. Exploiting the putative Neoproterozoic atmospheric composition (the “standard model”) envisaged by Claire et al (7), sulfur-species leave the atmosphere unequally divided between three exit channels. The model predicts that aerosol exit channels (SO_4 and S_8) feature fairly homogeneous $\Delta^{36}\text{S}/\Delta^{33}\text{S}$ signatures irrespective of the height of their tropospheric genesis. By contrast, the predicted $\Delta^{36}\text{S}/\Delta^{33}\text{S}$ ratios communicated to SO_2 vary substantially through the troposphere. SO_2 exits the atmosphere primarily dissolved in rainwater, so homogenization likely precludes the expression of the modeled $\Delta^{36}\text{S}/\Delta^{33}\text{S}$ variability ([Figures 4–5](#)). Aerosol species, by contrast, should serve as more instantaneous vectors carrying the entire range of $\Delta^{36}\text{S}/\Delta^{33}\text{S}$ to the Earth’s surface, resulting in spatial variability independent of atmospheric chemistry. Consequently, the modeled $\Delta^{36}\text{S}/\Delta^{33}\text{S}$ stability in aerosols is reassuring, advocating $\Delta^{36}\text{S}/\Delta^{33}\text{S}$ ratios as a conservative parameter reflective of a given atmospheric state; that, unlike the absolute S-MIF magnitude (32), would be unlikely to display significant widespread spatial variability under a truly global atmospheric state. This fits well with the stable background $\Delta^{36}\text{S}/\Delta^{33}\text{S}$ (-0.9) that is observed

throughout the majority of the 100 m (11.7 ± 3.3 Myr; [SI Appendix](#)) of examined core ([Figure 1](#)), and the wider Archean record (19).

The utility of $\Delta^{36}\text{S}/\Delta^{33}\text{S}$ ratios is extended via examination of [Figure 4B](#). Here, we present results from 22 distinct model atmospheres where the total volcanic sulfur flux was varied over two orders of magnitude. This experiment alters the atmospheric redox state, enhancing the relative importance of the S_8 exit-channel in the more sulfur-laden atmospheres. [Figure 4B](#) shows that within each model atmosphere the $\Delta^{36}\text{S}/\Delta^{33}\text{S}$ ratios of all exit-channels remain homogenous (± 0.1), in-turn supporting our claim that $\Delta^{36}\text{S}/\Delta^{33}\text{S}$ reflects the instantaneous state of atmospheric chemistry. The range and systematic decrease in $\Delta^{36}\text{S}/\Delta^{33}\text{S}$ observed between simulations (+0.2 to -0.4) highlights the sensitivity of $\Delta^{36}\text{S}/\Delta^{33}\text{S}$ ratios to atmospheric composition, advocating $\Delta^{36}\text{S}/\Delta^{33}\text{S}$ as a promising atmospheric probe—A conclusion that extends beyond both the chosen experiment (sulfur loading) and our predicted magnitudes.

To examine the ability of an organic haze to modulate $\Delta^{36}\text{S}/\Delta^{33}\text{S}$, we varied the O_2 and CH_4 fluxes (7, 10) to create two different hazy states, ([Models 1 & 3 in Figure 5B & 5D](#)) along with an additional clear-skies atmospheric state ([Model 2 in Figure 5C](#)). Similar to the cases presented previously ([Figure 4A](#)), the incorporation of the new cross-sections (33) causes the $\Delta^{33}\text{S}$ predictions to deviate from those presented previously (7), qualitatively approximating the geological record. Our simulated hazy atmospheric states produce $\Delta^{36}\text{S}/\Delta^{33}\text{S}$ slopes (+0.19, [Figure 5B](#) and -0.52, [Figure 5D](#)), which differ from the clear-skies simulation (-0.04, [Figure 5C](#)). The clear-skies simulation in [Figure 5C](#) has distinct, but broadly similar, boundary conditions to the “standard atmosphere” ([Figure 4A](#); 7) so their similar $\Delta^{36}\text{S}/\Delta^{33}\text{S}$ provides additional confidence that $\Delta^{36}\text{S}/\Delta^{33}\text{S}$ slopes are the product of specific atmospheric states, and do not vary widely with minor fluctuations in atmospheric state. We stress again that the absolute values of these predictions are preliminary and will likely change with additional model complexity ([SI Appendix](#)). Our approach here is not sufficient to make the claim that haze is uniquely responsible for variations in the $\Delta^{36}\text{S}/\Delta^{33}\text{S}$ slope from -0.9 to -1.5. Rather, our more simple aim is to test the assertion that atmospheric reaction rates, exit channels and UV transparency vary sufficiently underneath a hazy atmosphere to modulate the $\Delta^{36}\text{S}/\Delta^{33}\text{S}$ ratios (7-10). The predicted uniformity of $\Delta^{36}\text{S}/\Delta^{33}\text{S}$ ratios, expressed in all atmospheric exit channels, ultimately facilitates transmission from the atmosphere where they may be preserved in the geological record (8, 9, 18)—a key prediction of the haze hypothesis. Furthermore, the different $\Delta^{36}\text{S}/\Delta^{33}\text{S}$ ratios produced under different atmospheric hazy regimes provides support to the idea that hazes in different parts of Earth history (e.g., before

and after substantial biospheric O₂ fluxes) might yield unique S-MIF signatures (cf. [Figures 5B and 5D](#); 8).

A caveat to these inferences hinges on pyrite genesis, the global vs. regional extent of the haze, and the photochemical origin of the pyrite-sulfur precursor. Under a global hazy atmospheric configuration, after mixing into the seawater sulfate reservoir, putative hazy-type $\Delta^{36}\text{S}/\Delta^{33}\text{S}$ ratios (-1.5) would be preserved within pyrite independent of its initial sulfur source (e.g., sulfate or elemental sulfur; [Figures 4 & 5](#)). If regional haze development were possible, then conceivably pyrite could have inherited either a typical Archean $\Delta^{36}\text{S}/\Delta^{33}\text{S}$ (-0.9) or a steeper hazy-type $\Delta^{36}\text{S}/\Delta^{33}\text{S}$ (-1.5). Here, elemental sulfur would have carried the atmospheric $\Delta^{36}\text{S}/\Delta^{33}\text{S}$, and thus the localized instantaneous chemical state directly to pyrite. Contrastingly, pyrite produced from seawater sulfate would be expected to preserve a globally integrated signal, facilitated via oceanic mixing. Therefore, sulfate-sourced pyrite could carry a slope more characteristic of haze beneath a localized clear-skies atmospheric regime. Unfortunately, the current dataset displays exclusively positive $\Delta^{33}\text{S}$ ([Figures 2, SI Appendix, Fig. S2](#)), thus precluding a definitive appraisal of the precursor sulfur (18) in this particular C-S anomaly. Given that our pyrite record is derived from predominantly sulfur aerosols, reflecting instantaneous atmospheric chemistry, the shift in $\Delta^{36}\text{S}/\Delta^{33}\text{S}$ indicates core GKF01 was deposited beneath a hazy-sky, consistent with the observed C- and S-isotope covariation ([Figures 1 & 3A](#)).

CONSTRAINING THE TIMING AND DRIVERS OF ATMOSPHERIC HAZE FORMATION

These geochemical and computational arguments lend credence to the haze hypothesis. Accordingly, we interpret the C-S anomaly as a chemostratigraphic marker of atmospheric haze development. The well-defined structure of the high-resolution C-S anomaly ([Figure 1](#)) allows us to extract time constraints to reveal the tempo and duration of an inferred episode of haze development. Utilizing existing radiometric age constants (36-40; [SI Appendix](#)), and assuming linearity, application of average sedimentation rates ([SI Appendix](#)) suggest that haze persisted for 1.4 ± 0.4 Myr, attaining maximum haze thickness (lowest $\Delta^{36}\text{S}/\Delta^{33}\text{S}$) over 0.3 ± 0.1 Myr (3 m). Adopting these temporal constraints, even acknowledging the potential uncertainties of our approach (see [SI Appendix](#) for derivation and uncertainties), the development of Neoproterozoic atmospheric haze is inconsistent with rapid release of methane from a standing methane reservoir (such as methane hydrates), and requires a more sustained methane flux to the atmosphere.

While contemporary sedimentary methane production is substantial, little escapes to the ocean-atmosphere system owing to efficient consumption by either aerobic methanotrophs,

or by a consortium of anaerobic methanotrophs and sulfate reducers (AOM) at the sulfate-methane transition zone (41-43). Nevertheless, within the oxygen- and sulfate-starved Neoproterozoic oceans (44-46) methanogens would have proliferated, whilst methanotrophs and AOM would have been spatially restricted. Correspondingly, enhanced Neoproterozoic methanogenesis would have likely translated into elevated atmospheric CH₄ fluxes (41-43), supporting large background Archean CH₄ concentrations (7, 10, 20, 21, 41, 47). When the CH₄:CO₂ mixing ratio exceeded a critical threshold of ~ 0.1, this CH₄ flux would have formed an organic-rich hydrocarbon haze (9, 10, 20, 47), although the regional/global extent of these haze(s) require further study.

Methanogens feature a complex biochemistry dependent on nickel-based metallo-enzymes (48), which they use to produce methane at the expense of simple carbon compounds and molecular hydrogen (49, 50). Although reconstructed marine nickel concentrations suggest that post-2.7 Ga oceans were nickel limited (49, 50), it is improbable that nickel *alone* was a stimulus for episodically heightened methane production necessary for haze production. Neoproterozoic oceanic nickel depletion has been attributed to long-term unidirectional mantle cooling, changing the chemical composition of igneous rocks and concomitant marine nickel delivery (49, 50). In contrast, haze formation was geologically rapid, and occurred repeatedly in the prelude to the GOE (8, 9), thus requiring a recurrent, yet geologically short-lived, driver. While it is feasible that episodic volcanism could supply reactive igneous rocks, secular mantle cooling should have ensured their nickel content was progressively lower (49, 50). Perhaps more importantly, it is difficult to envisage a *solely* volcanic/hydrothermal driver that effectively decouples nickel delivery from other bio-essential elements (e.g., P, N, Fe, Mo et cetera; 13).

Alternatively, episodic top-down stimulation of the entire biosphere, via enhanced primary productivity in the surface waters, could provide a more satisfactory trigger for haze development. This inference is supported by relatively high total organic-carbon (TOC) abundances ($\geq 2\%$) within the C-S anomaly (Figure 3B) compared to the Neoproterozoic average (1.5 ± 1.3 Wt. %; 51). Although high TOC abundances could reflect either diminished dilution by carbonate, enhanced productivity or preservation, the consistently low Fe_{HR}/Fe_T (< 0.38) ratios observed during the C-S anomaly (Figure 1B), suggest that oxic sedimentation persisted³

³ Summation of the oxic (Fe_{carb}, Fe_{ox} and Fe_{mag}) and anoxic Fe extractions (Fe_{py}) defines the highly reactive Fe pool (Fe_{HR} = Fe_{carb} + Fe_{ox} + Fe_{mag} + Fe_{py}), which when normalized to the total Fe pool (Fe_T) and Fe_{py} permits distinction between oxic (Fe_{HR}/Fe_T = < 0.22), ferruginous (Fe_{HR}/Fe_T = > 0.38 and Fe_{py}/Fe_{HR} = < 0.7) and euxinic Fe_{HR}/Fe_T = > 0.38 and Fe_{py}/Fe_{HR} = > 0.8) depositional conditions. Details of mineral phases that comprise these operationally defined

(9, 15), arguing against a preservational control. Contrasting redox inferences gleaned from the S-MIF and the Fe-speciation records further implicate marine productivity with atmospheric haze development. Here the low Fe_{HR}/Fe_T (< 0.38) ratios, in concert with limited enrichments in redox sensitive trace metals (e.g. Mo, Re and U; 15), signal mildly oxic sedimentation against an anoxic atmospheric backdrop (Figure 1b). Given that atmospheric models insinuate O_2 residence times on the order of a few hours (7) and extremely reducing tropospheric conditions, these data can only be reconciled by oxygenic photosynthesis (15) creating locally oxygenated water column conditions and the development of an oxygen oasis (52). The production of oxygen and organic matter in surface environments and their destruction in deeper waters, the sediment–water interface and below, had the potential to spatially decouple oxygen and methane production; thereby, offering a mechanism where methane could have escaped water column reoxidation and contributed to the atmospheric methane burden.

Excluding a facies control on the observed TOC increase is more difficult. The deepening experienced during the mudstone deposition probably inhibited carbonate deposition via isolation from the photic zone (23), hence reducing the dilutive effects of the biogenic carbonates during the C-S anomaly. That said, the small-intercalated mudstones in the basal part of the examined section (< 840 m) represent the same facies change, yet do not display the isotopic covariation that defines the C-S anomaly. This difference we explain as a function of scale: The mudstone containing the C-S anomaly has known lateral facies equivalents in core GKP01 (15, 23, 53), so independent of dilution-type effects, TOC-rich sediments were deposited across a larger area of the Griqualand West basin during the C-S anomaly. Thus increased TOC deposition could have supplied ample organic carbon to fuel regionally pervasive methanogenesis, potentially enhancing methane fluxes to the atmosphere. Importantly, consistent with the predictions of atmospheric simulations (7), the persistence of large magnitude S-MIF with changing $\Delta^{36}S/\Delta^{33}S$ (Figure 2; SI Appendix, Fig. S1) demonstrates that the atmosphere remained essentially oxygen free (1-3, 6, 7, 10) despite evidence for enhanced oxygen production (9, 15). Apparently the global sinks of water column reductants (e.g. Fe^{2+} ; 4), combined with reduced atmospheric gases (e.g., H_2 , CH_4), were still sufficient to prevent atmospheric oxygenation at this time (7, 10).

Deciphering the ultimate stimulus for the inferred biospheric invigoration, and associated ecological shifts, remains difficult, yet given the persistence of large magnitude S-MIF (Figures

Fe pools and the empirically threshold values that separate each redox regime are given in the SI Appendix.

1–2, SI Appendix, Fig. S2), there is no need to invoke planetary scale oxidative weathering by free atmospheric O₂ (13, 14). Alternate mechanisms such as episodic chemical weathering driven by changes in climate and/or tectonics could directly, or indirectly (via changes in ocean circulation and upwelling efficiency), have delivered the necessary nutrients to the photic zone over widespread areas. Additionally, the emergence and proliferation of terrestrial life (51) should have also revolutionized weathering efficiency via ground level oxidative weathering (54), providing another mechanism to flux nutrients (e.g., P and bio-essential trace elements), along with sulfate to the ocean, without any significant leak of O₂ to the atmosphere.

Pyrite $\delta^{34}\text{S}$ values are lowest at the base of the C-S anomaly ($\sim -15\text{‰}$) before stabilizing to values close to those reconstructed from contemporaneous carbonate-associated sulfate from the Campbellrand carbonate platform (Figures 1, 3C; 55;). While these few ^{34}S depleted samples could easily reflect changes in sediment-housed microbial sulfur cycling and associated pyrite formation (19, 56), these data can also be reconciled with an initial weathering pulse delivering sulfate, and presumably other nutrients, to the biosphere. Beyond the fortuitous placement of the low $\delta^{34}\text{S}$ at the base of the C-S anomaly within an otherwise stable $\delta^{34}\text{S}$ record (Figures 1, 3C), unequivocal discrimination between these two potential explanations of the $\delta^{34}\text{S}$ data is challenging on the basis of bulk SF₆ measurements alone. Enigmatically, however, radiogenic $^{187}\text{Os}/^{188}\text{Os}_i$ ratios have recently been reported from the Mt. McRae shale, which can only be reconciled with crustal ^{187}Os ingrowth via β^- -decay of ^{187}Re , followed by remobilization and delivery to the marine reservoir (14). The Mt. McRae succession is perhaps one of the most celebrated Archean sedimentary successions, containing the ~ 2.5 Ga trace-element enrichments that were interpreted to represent pre-GOE whiffs of oxygen (13). Interestingly, as noted by Zerkle et al. (9), the upper Mt. McRae shale also features a change in $\Delta^{36}\text{S}/\Delta^{33}\text{S}$ to lower values (57), which is broadly associated with a change in $\delta^{13}\text{C}_{\text{Org}}$ —exhibiting some interesting parallels with the data presented herein. Unfortunately the Mt. McRae shale data are of insufficient resolution to make meaningful comparisons with our own, and no Re-Os data exist for the C-S anomaly examined in Figure 1. Clearly further targeted SF₆ and SIMS analysis, coupled with the application of sensitive radiogenic isotope tracers (e.g. Re-Os; 58), to this and other C-S anomalies (8, 9), has the potential to elucidate the source of the nutrients (weathering vs. oceanic nutrient redistribution) and should be a fruitful avenue of future research.

From an Earth system perspective, low seawater sulfate concentrations were likely an important prerequisite for haze formation, allowing methane to escape AOM in the sediment

pile and enter the atmosphere. The Neoproterozoic oceans as a whole are inferred to have had historically low sulfate concentrations (16, 45), poisoning the biosphere at a tipping point, allowing the balance between methane production and consumption to shift rapidly following pulses of marine fertilization and attendant sedimentary carbon delivery (8). Consequently, enhanced productivity would be expected to strengthen methane production, creating inflections in the $\delta^{13}\text{C}$ isotope record that are only coupled with changes in $\Delta^{36}\text{S}/\Delta^{33}\text{S}$ when methane fluxes are sufficient to affect atmospheric chemistry. Eventually, however, enhanced terrestrial colonization (51, 54), combined with increasing biological oxygen production (9, 15) and waning availability of residual reductants (e.g., Fe^{2+}), would have changed the marine budgets of electron acceptors (e.g. sulfate; 51), curbing biogenic methane fluxes via enhanced AOM (43), and ultimately changing the atmospheric response to biospheric stimulation (13, 15).

HAZE FORMATION AS A HARBINGER OF PLANETARY OXIDATION?

Biogenic methane production has been proposed as an efficient hydrogen shuttle to the exosphere (41). Empirical studies throughout the solar system reveal that multiple processes combine to enable hydrogen escape from the upper atmosphere at its maximum theoretical rate (59), meaning that planetary hydrogen loss can be approximated by the diffusive supply of H-bearing compounds from the stratosphere (e.g., H_2 , H_2O , CH_4). While freeze-distillation confines water vapor to the troposphere, methane escapes Earth's cold-trap and supplies hydrogen to the stratosphere through photolysis, which can be lost instantaneously to space—irreversibly shedding reducing power and potentially explaining how the Earth's surficial environment became irreversibly oxidized over long timescales (41, 59).

The abrupt change in $\Delta^{36}\text{S}/\Delta^{33}\text{S}$ correlated to a decrease in sedimentary $\delta^{13}\text{C}_{\text{Org}}$ seen in the C-S anomaly (Figure 1B; 3) demonstrates a rapid change in atmospheric chemistry, which we have interpreted to represent the development of a hydrocarbon haze formed at elevated methane concentrations. As such, our data and models provide support for the presence of substantial methane in the Archean atmosphere, confirming predictions made in multiple theoretical studies (3, 20, 41-43, 47, 59). Our previous work (8, 9, 17, 18), and the work of others (57), has shown that similar tandem decreases in $\Delta^{36}\text{S}/\Delta^{33}\text{S}$ and $\delta^{13}\text{C}_{\text{Org}}$ occur in other Neoproterozoic strata, suggesting the Neoproterozoic atmospheric composition was dynamic, and atmospheric haze development was potentially frequent in the overture to the GOE. Experimental data (60, 61) and photochemical models (7, 9, 10, 20, 47) both predict that hydrocarbon hazes form when $\text{CO}_2:\text{CH}_4$ mixing ratios exceed ~ 0.1 . Given the strong dependency of hydrogen escape on atmospheric methane availability (41, 59), conceptually,

therefore, intervals of haze development could have served as intervals of heightened hydrogen loss, implicating more reduced atmospheric chemistry as a harbinger of planetary oxidation.

Catling *et al.* (41) performed three time-resolved calculations where they fixed $p\text{CO}_2$ (0.0003, 0.003 and 0.01 bar) and calculated the $p\text{CH}_4$ necessary to maintain a surface temperature of 290K against the evolving luminosity of the Archean sun. Using their Figure 1A, $p\text{CH}_4$ was calculated to approximate 950, 170 and 130 ppm when $p\text{CO}_2$ was fixed at 0.0003, 0.003 and 0.01 bar. Simplifying atmospheric pressure to approximate 1 bar equates to background $\text{CH}_4\text{:CO}_2$ mixing ratios of 3.16 (950 ppm/300 ppm), 0.06 (170 ppm/3000 ppm) and 0.01 (130 ppm/10000 ppm) for each scenario respectively. Excluding the first scenario because the climatically necessitated $\text{CH}_4\text{:CO}_2$ mixing ratio requires the development of a potentially improbably thick organic-haze (7, 9, 20, 47), leaves two clear skies solutions to explore. Assuming organic-haze forms when the $\text{CH}_4\text{:CO}_2$ mixing ratio exceeds 0.1, haze development in each scenario requires either a 1.67- (0.1/0.06) or 10- (0.1/0.01) fold increase in atmospheric methane concentrations, or a factor of 1.5–10 increase in planetary oxidation rate representing $2.6\text{--}18 \times 10^{12}$ moles O_2 equivalents yr^{-1} , assuming the background state was $1\text{--}1.5 \times 10^{12}$ moles O_2 yr^{-1} . Consequently, given our estimate of haze duration (1.4 ± 0.4 Myr; [SI Appendix](#)), a single episode of haze development could equate to a net gain of up to $\sim 2.6\text{--}18 \times 10^{18}$ moles of O_2 equivalents to the Earth system (41).

It is important to stress that the absolute gain of oxygen equivalents, or the rate of hydrogen loss, depends on both the composition of the atmosphere and on predictions of their resulting climate. Catling *et al.* (41) utilized the climate model of Pavlov and Kasting (62), which has a substantial error in the methane absorption coefficients as rectified by Haqq-Misra *et al.* (47). When combined with more recent predictions of greenhouse and anti-greenhouse cooling effects (63), Archean $p\text{CO}_2$ in excess of 0.01 is required to warm the planet in lieu of the lower solar luminosity (47). A higher $p\text{CO}_2$ would reduce the background $\text{CH}_4\text{:CO}_2$ mixing ratio, requiring a more substantial CH_4 flux to instigate haze formation. Logically, therefore, larger fluxes of CH_4 would promote greater hydrogen escape rates, with concomitant greater oxidative effect, rendering our estimates conservative. A more accurate and precise treatment is dependent on emerging modeling approaches, incorporating more appropriate particle physics and coupled climate modules to calculate accurate radiative transfer through hazy atmospheres (63). However, for now, the most appropriate models reconcile haze development with available geological evidence and suggest that run-away haze development was inhibited by self-shielding (i.e., haze prevents methane photolysis), implicating intricate

feedback systems between biological methane production, atmospheric chemistry and surface-incident UV radiation (63).

Assimilated, core GKF01 reveals a pronounced and stratigraphically systematic excursion towards low $\Delta^{36}\text{S}/\Delta^{33}\text{S}$ and $\delta^{13}\text{C}$ that requires a change in the composition of the atmosphere. This contests the notion of homogenous atmospheric chemistry across vast swaths of Archean time (64), while providing the strongest evidence to date that the Neoproterozoic was dynamic on million-year time scales. These atmospheric oscillations are best explained via a strong teleconnection between the biosphere and atmospheric chemistry, whereby increased nutrient availability instigated a biogeochemical cascade, prompting organic-haze formation. Episodic haze formation should have hastened hydrogen escape and likely acted as a counter-intuitive mechanism of generating significant oxidizing equivalents to the whole Earth System against an oxygen-free atmospheric backdrop.

METHODS. The geochemical data presented herein have been generated following established methodologies. Similarly, the photochemical model has been updated, via the inclusion of updated SO_2 -photodissociation cross-sections (33), from that developed in Claire et al. (7). Here we précis our approach, reserving a complete description for the [SI Appendix](#). Briefly: Sulfur isotope analysis was performed on purified SF_6 , following CRS pyrite distillation, at the University of Maryland (8, 9). Analytical uncertainties are estimated from the long-term reproducibility of Ag_2S fluorinations, and estimated to be 0.02, 0.008, and 0.20 ‰ (1 standard deviation, 1σ) for $\delta^{34}\text{S}$, $\Delta^{33}\text{S}$, and $\Delta^{36}\text{S}$ ratios, respectively. Organic carbon isotope and TOC data were generated at the JPL Astrobiogeochemistry Laboratory (abcLab) using 10 % (vol/vol) HCl decarbonated sample residues. The average reproducibility of $\delta^{13}\text{C}_{\text{Org}}$ and TOC sample duplicates was found to be ± 0.22 ‰ and 0.02 %, respectively. Iron speciation analyses were conducted at the University of St. Andrews, exploiting an empirically calibrated sequential extraction (65), as detailed in (66), with an extract precision of $\sim 5\%$ ([SI Appendix](#)).

ACKNOWLEDGMENTS. This study was supported financially by a Natural Environment Research Council Fellowship NE/H016805 (to A.Z.) and a Natural Environment Research Council Standard Grant NE/J023485 (to A.Z., M.C. and S.P.). Further financial support was generously provided via a SAGES Postdoctoral & Early Career Researcher Exchange grant and The Geological Society of London's Alan and Charlotte Welch Fund (to G.I.). For his work performed at the Jet Propulsion Laboratory, California Institute of Technology, KHW acknowledges the support of a grant from the National Aeronautics and Space Administration. JF acknowledges funding from the NASA Exobiology program (NNX12AD91G). Final drafting was completed under the auspices of Simons Foundation collaboration on the origins of life

at MIT. GI thanks SI, PI and CLH for their continued support. Finally, the patience and perseverance of two anonymous reviewers is credited for significantly improving this contribution.

References

1. Farquhar J, Bao H, & Thiemens M (2000) Atmospheric Influence of Earth's Earliest Sulfur Cycle. *Science* 289(5480):756-758.
2. Farquhar J, Savarino J, Airieau S, & Thiemens MH (2001) Observation of wavelength-sensitive mass-independent sulfur isotope effects during SO₂ photolysis: Implications for the early atmosphere. *J. Geophys. Res-Planets* 106(E12):32829-32839.
3. Pavlov AA & Kasting JF (2002) Mass-Independent Fractionation of Sulphur Isotopes in Archean Sediments: Strong evidence for an Anoxic Archean Atmosphere. *Astrobiology* 2(1):27-41.
4. Holland HD (2006) The oxygenation of the atmosphere and oceans. *Philos. Trans. R. Soc. Lond. B Biol. Sci.* 361(1470):903-915.
5. Bekker A, *et al.* (2004) Dating the rise of atmospheric oxygen. *Nature* 427(6970):117-120.
6. Farquhar J, Zerkle AL, & Bekker A (2011) Geological constraints on the origin of oxygenic photosynthesis. *Photosyn. Res.* 107(1):11-36.
7. Claire MW, *et al.* (2014) Modeling the signature of sulfur mass-independent fractionation produced in the Archean atmosphere. *Geochim. Cosmochim. Acta* 141:365-380.
8. Izon G, *et al.* (2015) Multiple oscillations in Neoproterozoic atmospheric chemistry. *Earth Planet. Sci. Lett.* 431:264-273.
9. Zerkle AL, Claire MW, Domagal-Goldman SD, Farquhar J, & Poulton SW (2012) A bistable organic-rich atmosphere on the Neoproterozoic Earth. *Nat. Geosci.* 5(5):359-363.
10. Kurzwil F, *et al.* (2013) Atmospheric sulfur rearrangement 2.7 billion years ago: Evidence for oxygenic photosynthesis. *Earth Planet. Sci. Lett.* 366:17-26.
11. Guo Q, *et al.* (2009) Reconstructing Earth's surface oxidation across the Archean-Proterozoic transition. *Geology* 37(5):399-402.
12. Luo G, *et al.* (2016) Rapid oxygenation of Earth's atmosphere 2.33 billion years ago. *Sci. Adv.* 2(5).
13. Anbar AD, *et al.* (2007) A Whiff of Oxygen Before the Great Oxidation Event? *Science* 317(5846):1903-1906.
14. Kendall B, Creaser RA, Reinhard CT, Lyons TW, & Anbar AD (2015) Transient episodes of mild environmental oxygenation and oxidative continental weathering during the late Archean. *Sci. Adv.* 1(10).
15. Kendall B, *et al.* (2010) Pervasive oxygenation along late Archean ocean margins. *Nat. Geosci.* 3(9):647-652.
16. Crowe SA, Dossing, L.N., Beukes, N.J., Bau, M., Kruger, S.J., Frei, R., Canfield, D.E. (2013) Atmospheric oxygenation three billion years ago. *Nature* 501:535-538.
17. Williford KH, *et al.* (2016) Carbon and sulfur isotopic signatures of ancient life and environment at the microbial scale: Neoproterozoic shales and carbonates. *Geobiology* 14(2):105-128.
18. Farquhar J, Cliff, J., Zerkle, A.L., Kamyshny, A., and Poulton, S.W., Claire, M., Adams, D., Harms, B. (2013) Pathways for Neoproterozoic pyrite formation constrained by mass-independent sulfur isotopes. *Proc. Natl. Acad. Sci. U.S.A.* 110(44):17638-17643.
19. Johnston DT (2011) Multiple sulfur isotopes and the evolution of Earth's surface sulfur cycle. *Earth-Sci. Rev.* 106(1-2):161-183.

20. Domagal-Goldman SD, Kasting JF, Johnston DT, & Farquhar J (2008) Organic haze, glaciations and multiple sulfur isotopes in the Mid-Archean Era. *Earth Planet. Sci. Lett.* 269(1–2):29-40.
21. Zahnle K, Claire M, & Catling D (2006) The loss of mass-independent fractionation in sulfur due to a Palaeoproterozoic collapse of atmospheric methane. *Geobiology* 4(4):271-283.
22. Thomazo C, Nisbet EG, Grassineau NV, Peters M, & Strauss H (2013) Multiple sulfur and carbon isotope composition of sediments from the Belingwe Greenstone Belt (Zimbabwe): A biogenic methane regulation on mass independent fractionation of sulfur during the Neoproterozoic? *Geochim. Cosmochim. Acta* 121(0):120-138.
23. Schröder S, Lacassie, J.P., Beukes, N.J., (2006) Stratigraphic and geochemical framework of the Agouon drill cores, Transvaal Supergroup (Neoproterozoic, South Africa). *S. Afr. J. Geol.* 109:23-54.
24. Ono SH, Kaufman AJ, Farquhar J, Sumner DY, & Beukes NJ (2009) Lithofacies control on multiple-sulfur isotope records and Neoproterozoic sulfur cycles. *Precambrian Res.* 169: 58-67.
25. Ono S, *et al.* (2003) New insights into Archean sulfur cycle from mass-independent sulfur isotope records from the Hamersley Basin, Australia. *Earth Planet Sci. Lett.* 213(1–2):15-30.
26. Eigenbrode JL & Freeman KH (2006) Late Archean rise of aerobic microbial ecosystems. *Proc. Natl. Acad. Sci. U.S.A* 103(43):15759-15764.
27. Thomazo C, Ader M, Farquhar J, & Philippot P (2009) Methanotrophs regulated atmospheric sulfur isotope anomalies during the Mesoproterozoic (Tumbiana Formation, Western Australia). *Earth Planet Sci. Lett.* 279(1–2):65-75.
28. Ono S, Wing B, Johnston D, Farquhar J, & Rumble D (2006) Mass-dependent fractionation of quadruple stable sulfur isotope system as a new tracer of sulfur biogeochemical cycles. *Geochim. Cosmochim.* 70(9):2238-2252.
29. Roerdink DL, Mason PRD, Whitehouse MJ, & Brouwer FM (2016) Reworking of atmospheric sulfur in a Neoproterozoic hydrothermal system at Londozi, Barberton Greenstone Belt, Swaziland. *Precambrian Res.* 280:195-204.
30. Canfield DE, Farquhar J, & Zerkle AL (2010) High isotope fractionations during sulfate reduction in a low-sulfate euxinic ocean analog. *Geology* 38(5):415-418.
31. Oduro H, *et al.* (2011) Evidence of magnetic isotope effects during thermochemical sulfate reduction. *Proc. Natl. Acad. Sci. U.S.A* 108(43):17635-17638.
32. Halevy I (2013) Production, preservation, and biological processing of mass-independent sulfur isotope fractionation in the Archean surface environment. *Proc. Natl. Acad. Sci. U.S.A* 110(44):17644-17649.
33. Endo Y, *et al.* (2015) Photoabsorption cross-section measurements of ³²S, ³³S, ³⁴S, and ³⁶S sulfur dioxide from 190 to 220 nm. *J Geophys. Res-Atmos.* 120(6):2546-2557.
34. Lyons JR (2009) Atmospherically-derived mass-independent sulfur isotope signatures, and incorporation into sediments. *Chem. Geol.* 267(3–4):164-174.
35. Danielache SO, Eskebjerg C, Johnson MS, Ueno Y, & Yoshida N (2008) High-precision spectroscopy of ³²S, ³³S, and ³⁴S sulfur dioxide: Ultraviolet absorption cross sections and isotope effects. *J Geophys. Res-Atmos.* 113(D17):D17314.
36. Knoll AH & Beukes NJ (2009) Introduction: Initial investigations of a Neoproterozoic shelf margin-basin transition (Transvaal Supergroup, South Africa). *Precambrian Res.* 169(1–4):1-14.
37. Altermann W & Nelson DR (1998) Sedimentation rates, basin analysis and regional correlations of three Neoproterozoic and Palaeoproterozoic sub-basins of the Kaapvaal craton as inferred from precise U–Pb zircon ages from volcanoclastic sediments. *Sediment. Geol.* 120(1–4):225-256.

38. Barton ES, Altermann, W., Williams, I.S., Smith, C.B., (1994) U–Pb zircon age for a tuff in the Campbell Group, Griqualand West Sequence, South Africa: implications for early Proterozoic rock accumulation rates. *Gology* 22:343–346.
39. Gutzmer J & Beukes NJ (1998) High-grade manganese ores in the Kalahari manganese field: Characterization and dating of the ore forming events. in *Unpublished Report*, (Rand Afrikaans University, Johannesburg), p 221.
40. Sumner DY & Bowring SA (1996) U–Pb geochronologic constraints on deposition of the Campbellrand Subgroup, Transvaal Supergroup, South Africa. *Precambrian Res.* 79(1–2):25–35.
41. Catling DC, Zahnle KJ, & McKay CP (2001) Biogenic Methane, Hydrogen Escape, and the Irreversible Oxidation of Early Earth. *Science* 293(5531):839–843.
42. Kharecha P, Kasting J, & Siefert J (2005) A coupled atmosphere–ecosystem model of the early Archean Earth. *Geobiology* 3(2):53–76.
43. Beal EJ, Claire MW, & House CH (2011) High rates of anaerobic methanotrophy at low sulfate concentrations with implications for past and present methane levels. *Geobiology* 9(2):131–139.
44. Crowe SA, *et al.* (2014) Sulfate was a trace constituent of Archean seawater. *Science* 346(6210):735–739.
45. Zhelezinskaia I, Kaufman AJ, Farquhar J, & Cliff J (2014) Large sulfur isotope fractionations associated with Neoproterozoic microbial sulfate reduction. *Science* 346(6210):742–744.
46. Guy BM, *et al.* (2012) A multiple sulfur and organic carbon isotope record from non-conglomeratic sedimentary rocks of the Mesoproterozoic Witwatersrand Supergroup, South Africa. *Precambrian Res.* 216–219:208–231.
47. Haqq-Misra JD, Domagal-Goldman SD, Kasting PJ, & Kasting JF (2008) A revised, hazy methane greenhouse for the Archean Earth. *Astrobiology* 8(6):1127–1137.
48. da Silva JJRF & Williams RJP (1991) *The Biological Chemistry of the Elements: The Inorganic Chemistry of Life* (Oxford University Press).
49. Konhauser KO, *et al.* (2009) Oceanic nickel depletion and a methanogen famine before the Great Oxidation Event. *Nature* 458(7239):750–753.
50. Konhauser KO, *et al.* (2015) The Archean Nickel Famine Revisited. *Astrobiology* 15(10):804–815.
51. Stüeken EE, Catling DC, & Buick R (2012) Contributions to late Archean sulphur cycling by life on land. *Nat. Geosci.* 5(10):722–725.
52. Olson SL, Kump LR, & Kasting JF (2013) Quantifying the areal extent and dissolved oxygen concentrations of Archean oxygen oases. *Chem. Geol.* 362:35–43.
53. Sumner DY & Beukes NJ (2006) Sequence stratigraphic development of the Neoproterozoic Transvaal carbonate platform, Kaapvaal Craton, South Africa. *S. Afri. J. Geol.* 109:11–22.
54. Lalonde SV & Konhauser KO (2015) Benthic perspective on Earth’s oldest evidence for oxygenic photosynthesis. *Proc. Natl. Acad. Sci. U.S.A* 112(4):995–1000.
55. Paris G, Adkins JF, Sessions AL, Webb SM, & Fischer WW (2014) Neoproterozoic carbonate–associated sulfate records positive $\Delta^{33}\text{S}$ anomalies. *Science* 346(6210):739–741.
56. Bradley AS, *et al.* (2016) Patterns of sulfur isotope fractionation during microbial sulfate reduction. *Geobiology* 14(1):91–101.
57. Kaufman AJ, *et al.* (2007) Late Archean Biospheric Oxygenation and Atmospheric Evolution. *Science* 317(5846):1900–1903.
58. Cohen AS (2004) The rhenium–osmium isotope system: applications to geochronological and palaeoenvironmental problems. *J. Geol. Soc. London* 161(4):729–734.

59. Zahnle KJ, Catling DC, & Claire MW (2013) The rise of oxygen and the hydrogen hourglass. *Chem. Geol.* 362:26-34.
60. Trainer MG, *et al.* (2006) Organic haze on Titan and the early Earth. *Proc. Natl. Acad. Sci. U.S.A* 103(48):18035-18042.
61. Hasenkopf CA, *et al.* (2010) Optical properties of Titan and early Earth haze laboratory analogs in the mid-visible. *Icarus* 207(2):903-913.
62. Pavlov AA, Kasting JF, Brown LL, Rages KA, & Freedman R (2000) Greenhouse warming by CH₄ in the atmosphere of early Earth. *J. Geophys Res-Planets* 105(E5):11981-11990.
63. Arney G, Domagal-Goldman, S., Meadows, V., Wolf, E., Schwieterman, E., Charnay, B., Hebrard, E., Trainer, M. & Claire, M (2016) The Pale Orange Dot: The spectrum and habitability of hazy Archean Earth. *Astrobiology* 16(11):1-27.
64. Thomassot E, O'Neil J, Francis D, Cartigny P, & Wing BA (2015) Atmospheric record in the Hadean Eon from multiple sulfur isotope measurements in Nuvvuagittuq Greenstone Belt (Nunavik, Quebec). *Proc. Natl. Acad. Sci. U.S.A* 112(3):707-712.
65. Poulton SW & Canfield DE (2005) Development of a sequential extraction procedure for iron: implications for iron partitioning in continentally derived particulates. *Chem. Geol.* 214(3-4):209-221.
66. Poulton, SW, Fralick, PW, Canfield, DE, (2010) Spatial variability in oceanic redox structure 1.8 billion years ago. *Nat. Geosci.* 3:486-490.
67. Poulton SW & Canfield DE (2011) Ferruginous Conditions: A Dominant Feature of the Ocean through Earth's History. *Elements* 7(2):107-112.
68. Fischer WW, *et al.* (2009) Isotopic constraints on the Late Archean carbon cycle from the Transvaal Supergroup along the western margin of the Kaapvaal Craton, South Africa. *Precambrian Res.* 169(1-4):15-27.
69. Eriksson PG, Altermann W, & Hartzler FJ (2006) *The Geology of South Africa*, (eds) Johnson MR, Anhaeusser, C.R., and Thomas, R.J. Geological Society of South Africa, Johannesburg/Council for Geoscience, Pretoria, pp 237-260.
70. Canfield DE, Raiswell R, Westrich JT, Reaves CM, & Berner RA (1986) The use of chromium reduction in the analysis of reduced inorganic sulfur in sediments and shales. *Chem. Geol.* 54(1-2):149-155.
71. Clarkson MO, Poulton SW, Guilbaud R, & Wood RA (2014) Assessing the utility of Fe/Al and Fe-speciation to record water column redox conditions in carbonate-rich sediments. *Chem. Geol.* 382:111-122.
72. Raiswell R & Canfield DE (1998) Sources of iron for pyrite formation in marine sediments. *Am. J. Sci.* 298(3):219-245.
73. Anderson TF & Raiswell R (2004) Sources and mechanisms for the enrichment of highly reactive iron in euxinic Black Sea sediments. *Am. J. Sci.* 304(3):203-233.
74. Poulton SW & Raiswell R (2002) The low-temperature geochemical cycle of iron: From continental fluxes to marine sediment deposition. *Am. J. Sci.* 302(9):774-805.
75. Cumming VM, Poulton SW, Rooney AD, & Selby D (2013) Anoxia in the terrestrial environment during the late Mesoproterozoic. *Geology* 41(5):583-586.
76. Poulton SW, *et al.* (2015) A continental-weathering control on orbitally driven redox-nutrient cycling during Cretaceous Oceanic Anoxic Event 2. *Geology* 43(11):963-966.
77. März C, *et al.* (2008) Redox sensitivity of P cycling during marine black shale formation: Dynamics of sulfidic and anoxic, non-sulfidic bottom waters *Geochim. Cosmochim. Acta* 72(15):3703-3717.

78. Pavlov AA, Kasting JF, Eigenbrode JL, & Freeman KH (2001) Organic haze in Earth's early atmosphere: Source of low- ^{13}C Late Archean kerogens? *Geology* 29(11):1003-1006.
79. Claire MW, *et al.* (2012) The evolution of the solar flux from 0.1 nm to 160 μm : Quantitative estimates for planetary studies. *Astrophys. J.* 757:1-12.

Figures:

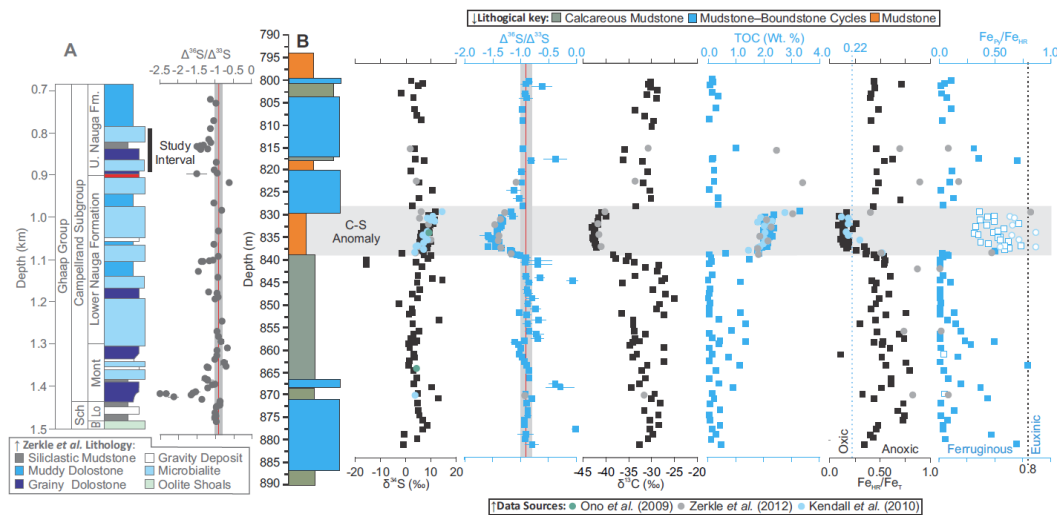


Figure 1 Pre-existing lithological and geochemical data from core GKF01 (9) combined with new high-resolution geochemical data. Panel A comprises the published low-resolution GKF01 $\Delta^{36}\text{S}/\Delta^{33}\text{S}$ record (9), the Neoproterozoic reference array (red line) and its ± 0.1 uncertainty envelope (grey vertical band; 8). Panel B features the new $\delta^{34}\text{S}$, $\Delta^{36}\text{S}/\Delta^{33}\text{S}$, $\delta^{13}\text{C}$, TOC and Fe-speciation ($\text{Fe}_{\text{HR}}/\text{Fe}_{\text{T}}$, $\text{Fe}_{\text{PY}}/\text{Fe}_{\text{HR}}$) data (squares) along with published data (filled circles; 9, 15, 24). The horizontal grey band signifies the C-S anomaly (see text). The vertical red line and grey envelope in the $\Delta^{36}\text{S}/\Delta^{33}\text{S}$ plot represent the Neoproterozoic reference array and its associated uncertainty (± 0.1 ; 8). Vertical lines in the Fe-speciation plots distinguish oxic from anoxic ($\text{Fe}_{\text{HR}}/\text{Fe}_{\text{T}} \geq 0.38$) and ferruginous from definitively euxinic ($\text{Fe}_{\text{PY}}/\text{Fe}_{\text{HR}} > 0.7$) water column conditions. The open symbols in the $\text{Fe}_{\text{HR}}/\text{Fe}_{\text{PY}}$ plot have $\text{Fe}_{\text{HR}}/\text{Fe}_{\text{T}} < 0.22$, signifying oxic sedimentation (9, 15, 67). Assimilating these observations, sedimentation during the examined interval was likely dynamic, with a generally ferruginous background state ($\text{Fe}_{\text{HR}}/\text{Fe}_{\text{T}} > 0.38$; $\text{Fe}_{\text{PY}}/\text{Fe}_{\text{HR}} < 0.7$), becoming oxygenated during the C-S anomaly ($\text{Fe}_{\text{HR}}/\text{Fe}_{\text{T}} < 0.22$; 15). The definition of Fe_{HR} , Fe_{PY} and Fe_{T} are footnoted[‡], whereas the derivation of the diagnostic Fe-speciation threshold values are given in the [SI Appendix](#). Analytical uncertainties (1 standard deviation, 1σ) are typically encompassed within each individual data point with the exception of a few $\Delta^{36}\text{S}/\Delta^{33}\text{S}$ ratios whose uncertainty was computed from larger of the internal or external 1σ uncertainties associated with the raw $\Delta^{33}\text{S}$ and $\Delta^{36}\text{S}$ data (9). The large-scale lithological log (A) follows that presented in Zerkle *et al.* (9), whereas the new data (B)

are plotted against the detailed sedimentary logs, which along with core photos are available online (<http://general.uj.ac.za/agouron/index.aspx>).

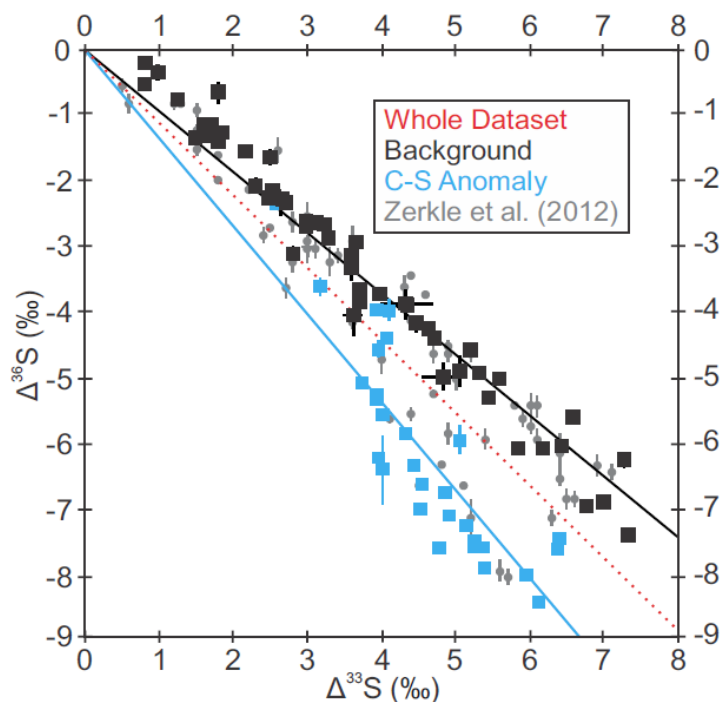


Figure 2 Quadruple S-isotope data from core GKF01 (A) with a schematic mixing scenario (B). $\Delta^{36}\text{S}$ versus $\Delta^{33}\text{S}$ trends for the new data (black and blue) superimposed on previously published data (grey circles; 9). Regressions are given through the whole dataset (red) as well as through the C-S anomaly (blue) and background (black). Uncertainties are plotted conservatively, using the larger of the internal or external uncertainty (1σ), and are consistently smaller than a single data point. The insert (B) schematically illustrates the range of $\Delta^{33}\text{S}$ and $\Delta^{36}\text{S}$ values that can be expressed in pyrite (shaded grey area) formed via mixing of sulfide derived from microbial sulfate reduction (open circles 3-4) with atmospherically derived S-MIF carried by sulfate (filled circle 1) and elemental sulfur (filled circle 2). The horizontal blue bar illustrates the $\Delta^{36}\text{S}$ - $\Delta^{33}\text{S}$ systematics of TSR derived sulfide. Note, biological activity has the potential to exert greater influence on $\Delta^{36}\text{S}/\Delta^{33}\text{S}$ when pyrite carries a negative $\Delta^{33}\text{S}$ (i.e. derived from sulfate) rather than a positive $\Delta^{33}\text{S}$ (29) as observed in the C-S anomaly (Figure 1) and mixing with TSR derived sulfide moves the $\Delta^{36}\text{S}/\Delta^{33}\text{S}$ to less negative values.

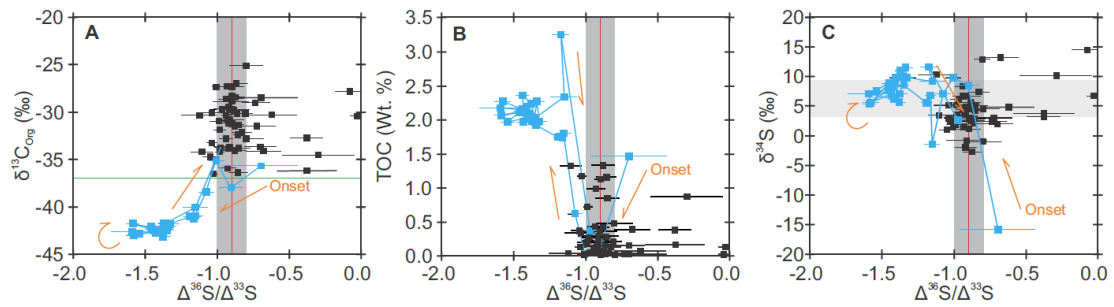


Figure 3 Carbon isotope ($\delta^{13}\text{C}$; **A**), TOC (**B**) and $\delta^{34}\text{S}$ (**C**) versus $\Delta^{36}\text{S}/\Delta^{33}\text{S}$ data from 800–900 m core depth in core GKF01. In each plot the data have been color coded, differentiating the background (black) from the C-S anomaly (blue), with orange arrows illustrating its temporal evolution. Vertical red lines in each plot give the average Neoproterozoic $\Delta^{36}\text{S}/\Delta^{33}\text{S}$ with a ± 0.1 uncertainty envelope (vertical grey bar; 8). The horizontal green line in panel A marks $\delta^{13}\text{C} = -37\text{‰}$, a threshold commonly used to identify methanotrophy (8, 9, 26). The horizontal grey bar in panel C represents the range of seawater $\delta^{34}\text{S}$ estimates derived from carbonate-associated sulfate (55). Typically analytical uncertainty is encompassed within the data points, with the exception of a few $\Delta^{36}\text{S}/\Delta^{33}\text{S}$ ratios as in [Figure 2](#).

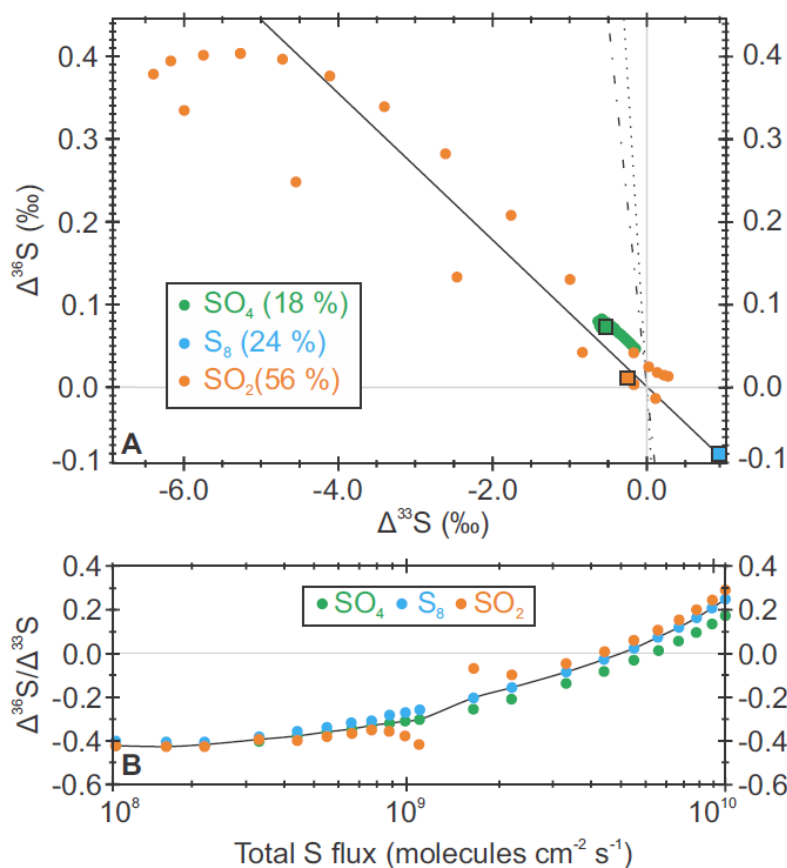


Figure 4 Photochemical $\Delta^{36}\text{S}$ and $\Delta^{33}\text{S}$ predictions for the “standard atmosphere” (7) under normal conditions (A) and with differential sulfur loading (B). Under standard atmospheric conditions, in Figure 4A, sulfur leaves the model atmosphere unequally divided between three exit channels (SO_2 , 56 %; S_8 , 24 % and SO_4 , 18 %). Values of $\Delta^{36}\text{S}/\Delta^{33}\text{S}$ are displayed for the entire troposphere (filled circles), with the large squares showing the ground-level signal carried by a specific exit channel combining both wet and dry deposition. Figure 4B recreates the experiment illustrated in Figures 6c–d in Claire et al. (7), where the total volcanic sulfur flux to the model atmosphere is varied over two orders of magnitude (10^8 – 10^{10} molecules $\text{cm}^{-2} \text{s}^{-1}$). The spatial distribution of atmospherically important species within the standard atmospheric framework is displayed in Figure 2 of Claire et al. (7) where the following boundary conditions were adopted: volcanic sulfur flux of 3.85×10^9 molecules $\text{cm}^{-2} \text{s}^{-1}$ (1 Tmole a^{-1}) at an $\text{H}_2\text{S}:\text{SO}_2$ ratio of 1:10 and a volcanic H_2 flux of 1×10^{10} molecules $\text{cm}^{-2} \text{s}^{-1}$ (3 Tmole a^{-1}). Fixed ground-level mixing ratios of 100 ppm and 10 ppb for CH_4 and O_2 , respectively. Carbon dioxide concentrations were fixed at 1 % at all heights and N_2 provided a total atmospheric pressure of 1 bar. Full details of the model, validation and its limitations are given in the [SI Appendix](#).

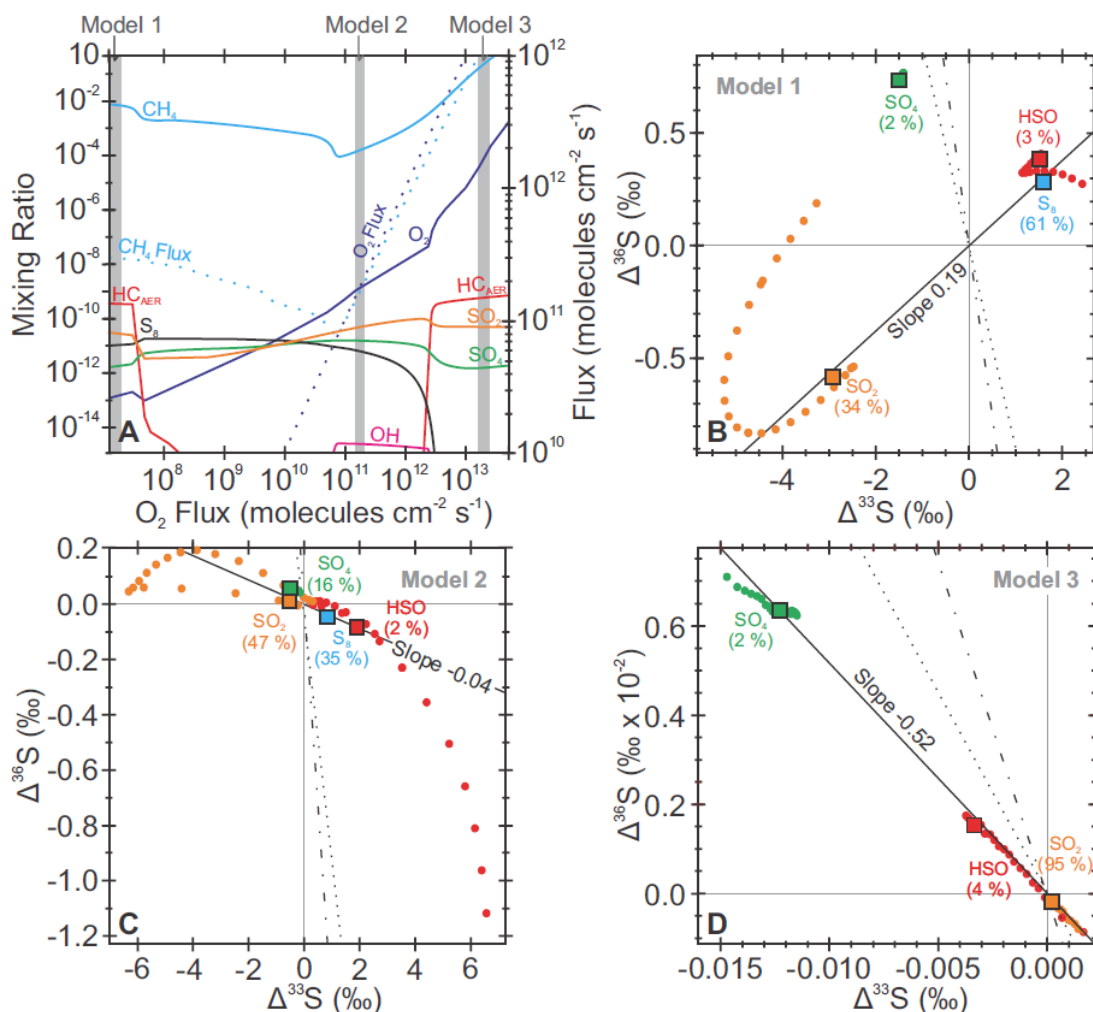


Figure 5 Simulated $\Delta^{36}\text{S}/\Delta^{33}\text{S}$ response to varying O_2 and CH_4 fluxes. Figure 5A shows the three distinct atmospheric states (Models 1–3, Figures 5B–5D) that were chosen to examine the effect of a hydrocarbon haze on atmospheric chemistry (numbered vertical grey bands Figure 5A): The first model simulates a thick hydrocarbon haze prior to the advent of oxygenic photosynthesis (Figure 5B), whereas the second and third models represent haze-free (Figure 5C) and hazy (Figure 5D) states after the advent of oxygenic photosynthesis (7, 10). Under each atmospheric regime (Figures 5B–5D) the $\Delta^{36}\text{S}/\Delta^{33}\text{S}$ carried by each atmospheric exit channel, at specific atmospheric height, is plotted as color-coded circles, whereas the atmospherically integrated signal (the ground-level value) of each vector is represented by a color-coded large square (Plots B–D). The relative importance of each exit labeled channel is given in parenthesis. In plot A the mixing ratios of atmospheric species are shown as solid lines (left axis), while fluxes are shown as dashed lines (right axis). In Figure 5B–5D the Archean reference array ($\Delta^{36}\text{S}/\Delta^{33}\text{S} = -0.9; 8$), the steepened slope reflecting the C-S anomaly (Figure 1) and the best fit to the simulated data are given by the dotted, dot-dashed and solid lines respectively. Full details of the model, validation and its limitations are given in the SI

Appendix. Zero $\Delta^{36}\text{S}$ and $\Delta^{33}\text{S}$ data are given as grey lines to illustrate the change in scale between Figure 5B–D.

ONLINE SUPPLEMENTARY MATERIAL – Izon et al., Biological Regulation of Atmospheric Chemistry En Route to Planetary Oxygenation

GEOLOGICAL SETTING AND AGE MODEL

The study that initially noted covariation between $\Delta^{36}\text{S}/\Delta^{33}\text{S}$ and $\delta^{13}\text{C}$ exploited samples from core GKF01 (Figure S1; 9), and focused on the basal Ghaap group, spanning the Boomplaas–Upper Nauga Formations (Figure 1). Core GKF01, and its companion core GKP01, was recovered southwest of Griquatown (Figure S1) capturing proximal to mid-platform slope sedimentation. Core GKF01 bottomed in the Boomplaas Formation of the Schmidtsdrif Subgroup, and recovered a complete record Schmidtsdrif–Campbellrand sediments; encompassing the Boomplaas and Lokammona Formations of the Schmidtsdrif Subgroup, overlain by the Monteville, Nauga and Klein Naute Formations of the Campbellrand Subgroup (Figure 1; 23, 36, 53).

In contrast to the Schmidtsdrif Subgroup, the Campbellrand Subgroup displays spatial heterogeneity within Griqualand West Basin, being subdivided into two facies domains (68, 69). Each domain features different sedimentary facies resulting from the basinal configuration and the paleowater depth; with shallow water facies (Ghaap Plateau facies) restricted to the north of Griquatown Fault Zone, and the deeper water (Prieska facies) equivalents to the south (Figures S1; 68, 69). Core GKF01 documents Prieska-type Transvaal sedimentation, whereas BH1-Sacha is further north and represents thicker, shallow-water, sedimentation. Despite the difference in stratigraphic nomenclature, $\Delta^{36}\text{S}/\Delta^{33}\text{S}$ – $\delta^{13}\text{C}$ covariation has been recorded in each core, suggesting the chemostratigraphic trends are insensitive to water-depth (an inference borne out by our new data). To better our understanding of haze formation we revisit core GKF01 and construct a high-resolution geochemical record from ~900–800m (Figures 1–3). We target this stratigraphic interval based on the initial work of Zerkle *et al.* (9). This is the youngest known C-S anomaly for which good core recovery exists but importantly it overlies the Kamden Iron formation (~905 m)—a prominent and pervasive stratigraphic marker—meaning our efforts should be directly traceable into other cores.

The chronostratigraphic framework for the Prieska–Koegas area, along the southwestern margin of the Kaapvaal craton, is developed predominately from SHRIMP U-Pb ages derived

from zircons concentrated from the various intercalated tuff beds. Within this framework the zircon population ages young systematically and show good agreement between studies (36-40). Knoll and Beukes (36) exploited the unusually large number of marker beds present in core GKP01 (companion core to GKF01) to correlate the core to outcrop-derived “type-profiles”, and exploit the existing precise U-Pb radiometric age constraints (see their Figure 8; ref. 36).

Although the tuff horizons in GKF01 are not as well documented as in GKP01, the proximity of the two cores (~24 km), combined with the presence of well-defined lithological, sequence stratigraphic and impactite horizons (23), allows us to develop a crude linear age-depth model. We use these age controls to place the first constraints on the duration of the C-S anomaly and hence an episode of Neoproterozoic hazes formation. The implications of these temporal constraints are discussed in the manuscript. Specifically, using the age constraints on Tuff 4 at ~905 m core depth beneath the Kamden member (2581 ± 9 Ma, ref. 39; 2588 ± 6 Ma, ref. 37) and Tuff 0 beneath Bruno’s band (2521 ± 3 Ma, ref 40; 2516 ± 4 Ma, ref. 37) at 325 m core depth results in a calculated compacted sedimentation rate (CSR) of 9.5 ± 2.5 m Myr⁻¹. Applying these estimates to our new chemostratigraphic record, suggests that the haze persisted for 1.4 ± 0.4 Myr (12.13 m), attaining maximum haze thickness in 0.3 ± 0.1 Myr (3 m).

We stress that while these time estimates are the first on haze formation they are subject to numerous sources of uncertainty and are reliant on poorly known sedimentation rates. The errors we have quoted above are simply propagated from those offered in the initial papers (36-40) and do not account for deviation from linear sedimentation. Deviation from linear sedimentation—our implicit assumption—could result from (i) facies dependent sedimentation rates, (ii) differential compaction histories (iii) instantaneous sedimentation (e.g. turbidites) and (iv) unrecognized sedimentary hiatuses. While there are no reports of hiatuses, sedimentary facies are observed to vary on a number of scales throughout core GKF01. The Nauga formation, for example, features pronounced cyclicity, with microbialite–slope carbonates couplets occasionally passing into siliciclastic mudstone. On a broader scale, in the basal part of GKF01, microbialite facies are more volumetrically important than in the younger part of the succession. Consequently, there is good reason to suspect slight deviation from linear behavior (23), with variable and scale-dependent sedimentation rates. To examine this potential scale dependency, we constructed CSRs over a longer stratigraphic interval (Lokammona–Klein Naute Formations). Here we adopt the age from the dated Lokammona tuff to constrain the age of the uppermost surface of Lokammona Formation at 1440 m core

depth (2650 ± 8 Ma, ref. 39), and repeat the same exercise as above. Taking these datums we calculate the CSR to be 8.5 ± 0.9 m Myr⁻¹, which is statistically inseparable from our previous estimate. This agreement, providing that there are no substantial unrecognized sedimentary hiatuses, suggests that that uncertainty implicit in radiometric age determinations dominates or age assignments. Given that the presented chronostratigraphic framework is unusually detailed, a reduction in these uncertainties will require precise dating of the core directly; thus circumnavigating complications involved with correlations to the regionally developed geochronology. **METHODOLOGY**

QUADRUPLE S-ISOTOPE DETERMINATION: Sedimentary sulfide phases were extracted via sequential reflux with 6 M HCl and acidified 1 M CrCl₂ (8). The first reduction step yielded operationally defined acid volatile sulfur (AVS) whereas the second stage reduced pyritic sulfur, which was precipitated as silver sulfide (8, 9, 70). The purified Ag₂S (1–3 mg) was reacted with a 10-fold excess of fluorine gas (F₂) at 250°C for approximately 8–12 hours in Ni bombs. The reaction product, sulfur hexafluoride (SF₆), was cryogenically separated from residual F₂ (at -196°C) and from HF and other trace contaminants (at -115°C), using liquid nitrogen (LN₂) and an ethanol-LN₂ slurry, respectively. Finally, the SF₆ was purified via gas chromatography using a composite column comprised of a type 5A molecular sieve (3.18 mm diameter, 1.8 m long), followed by a Hayes-Q™ column (3.18 mm diameter, 3.6 m long). Under these conditions SF₆ was eluted after ~13 minutes using a He carrier gas (20 mL min⁻¹ at 50°C) and the yield was quantified to > 95 %.

The S-isotope composition of the pure SF₆ was measured via DI-IRMS (Thermo-Finnigan MAT 253) using four collectors arranged to measure the intensity of SF₅⁺ ion beams at mass charge ratios (m/z) of 127, 128, 129, and 131 (³²SF₅⁺, ³³SF₅⁺, ³⁴SF₅⁺, and ³⁶SF₅⁺). Analytical uncertainties are estimated from the long-term reproducibility of Ag₂S fluorinations, and are deemed to be 0.02, 0.008, and 0.20 ‰ (1 standard deviation, 1σ) for δ³⁴S, Δ³³S, and Δ³⁶S ratios, respectively. The accuracy of the presented data was assessed via identical purification of IAEA S1 and S3 standards producing data inline with published accepted values (8, 9).

CARBONATE ABUNDANCE AND ORGANIC CARBON ISOTOPE: The carbonate-carbon fraction was quantitatively removed from homogenized sample powders via multiple overnight 10 % (vol/vol) HCl acid attacks, allowing the carbonate abundance to be calculated gravimetrically. The resulting carbonate free residues were then rinsed to neutrality using Mille-Q^(R) ultrapure-water (18.2 MΩ·cm) before being dried at 40°C at the University of St Andrews (8).

The dry sample residues were homogenized and weighed into tin cups ready for organic carbon isotope (δ¹³C_{Org}) and total organic carbon (TOC) determination at the JPL

Astrobiogeochemistry Laboratory (abcLab) over four analytical sessions. During each session, an acetanilide standard (Costech Analytical) was analyzed in multiple (n=8) to monitor external precision, linearity and instrument response for TOC calculation. Carbon-isotope data are expressed as ‰ deviations from the V-PDB standard, via normalization after duplicate analysis of NBS19 (1.95 ‰) and LSVEC (-46.6 ‰) within each analytical session. External reproducibility is deemed to be 0.07 ‰ (1 σ), based on the replicate analysis of between 1.5 and 4.5 μmol of acetanilide-C.

Initially 1 mg sample aliquots were analyzed with the intention to introduce $\sim 2 \mu\text{mol}$ C into the mass spectrometer. Many of these initial analyses yielded 1.5–4.5 μmol C; however, most (51 of 91) were analyzed a second time with variable sample weights to yield $\sim 2 \mu\text{mol}$ C. Average reproducibility of $\delta^{13}\text{C}_{\text{Org}}$ and TOC sample duplicates was found to be $\pm 0.22 \text{ ‰}$ and 0.02 %, respectively. Consequently, where available, the data are calculated and plotted as averages with their associated reproducibility.

SEDIMENTARTY FE-SPECIATION: Iron speciation analyses were conducted at the Department of Earth Sciences, University of St. Andrews to determine the paleoredox of the investigated samples (9). Highly reactive Fe (Fe_{HR}), comprising pyrite Fe and other Fe phases that are reactive to sulfide to form pyrite in the water column or during early diagenesis, were quantified via only minor modification from established techniques (65–67, 71). Briefly, 0.1 g of sample powder was exposed to acetic acid buffered (pH 4.5), 1 M sodium acetate solution at 50°C for 48 hours to liberate carbonate Fe (Fe_{Carb}), including siderite and ankerite. The leached residues were attacked for 2 hours at ambient temperature by 0.29 M sodium dithionite solution, buffered to pH 4.8 using a mixed 0.3/0.2 M acetic acid/sodium citrate solution, to target diagenetically reducible Fe oxides (Fe_{Ox}) such as goethite and hematite. Finally the remaining magnetite (Fe_{Mag}) was extracted with a mixed 0.2/0.17 M ammonium oxalate/oxalic acid solution. Iron concentrations were determined using Thermo Scientific iCAP 6300 inductively coupled plasma optical emission spectrometer after 20-fold dilution. Standardization was achieved using synthetic, matrix matched, 0–10 $\mu\text{g ml}^{-1}$ Fe standards. Reproducibility, based on 10 replicate extractions of PACS-2 is demonstrated to be better than 5 %; however, this is likely to be an underestimate of some low-Fe samples where analytical reproducibility is more likely to approximate 10 %.

The Ag_2S precipitated for S-isotope analysis allowed the final Fe-pool(s) to be quantified gravimetrically, with AVS representing monosulfides (FeS) and CRS representing pyrite (FeS_2), whose sum represents the inorganic sulfurized pool ($\text{Fe}_{\text{Py}} = \text{Fe}_{\text{AVS}} + \text{Fe}_{\text{CRS}}$). Repeat extraction of (n=6) demonstrates that reproducibility is better than 5% for sedimentary CRS distillation (70).

Comprehensive surveys of both contemporary (72) and Phanerozoic sediments (73) demonstrate that products of anoxic sedimentation generally have Fe_{HR}/Fe_T ratios above 0.38, and hence this is the diagnostic threshold used to discriminate between oxic and anoxic sedimentation (9, 15, 67). In detail, 0.38 is a conservative discriminator of anoxic deposition because ancient rocks deposited beneath an oxic water column feature lower Fe_{HR}/Fe_T ratios (0.14 ± 0.08 ; 74). Accordingly Fe_{HR}/Fe_T ratios below 0.22 are considered to unequivocally indicate an oxygenated water column, whereas intermediate Fe_{HR}/Fe_T (0.22–0.38) ratios remain ambiguous and could be a product of either oxic or anoxic deposition, and require careful examination to reach robust conclusions (65-67, 75). Differentiating whether anoxic sediments ($Fe_{HR}/Fe_T > 0.38$) were deposited under ferruginous or euxinic water column can be achieved by considering the extent of pyritization of the Fe_{HR} pool (65-67, 75-77). Modern euxinic environments have been used to set the upper limit for ferruginous deposition (Fe_{Py}/Fe_{HR} ; 74) however, the employed Fe extraction technique failed to adequately define the Fe_{Carb} and Fe_{Mag} pools (67), and recent work suggests that 70% pyritization of the Fe_{HR} pool ($Fe_{Py}/Fe_{HR} = 0.7$) may be a more appropriate threshold (65-67, 75-77).

The Fe-speciation proxy was originally developed to be applied to siliclastic sediments and has only recently been calibrated in carbonate-rich facies (71). Clarkson *et al.* (71), via analysis of modern and ancient samples, demonstrated that reliable redox inferences, using the aforementioned discriminators, can be made providing the analyte contains more than 0.5 Wt % Fe. These authors (71) also found via analysis of burial dolomites that the Fe-speciation proxy appears to be susceptible deep burial dolomitization, where there has been a source of mobile Fe during recrystallization. Our carbonate-rich samples contain more than 0.5 Wt. % Fe and therefore should encode reliable redox information. That said, we acknowledge that some of these samples have experienced dolomitization, which may have increased their Fe-contents. Accordingly we have opted to conservatively only place emphasis on the Fe-speciation data derived from the center of the C-S anomaly, which are derived from siliclastic lithologies and hence not influenced by dolomitization.

PHOTOCHEMICAL MODELING: The model used to predict and examine the utility of the $\Delta^{36}S/\Delta^{33}S$ parameter is updated from that presented previously by Claire *et al* (7). The 1-D photochemical model comprises 74 gas-phase species undergoing 392 photochemical reactions and includes vertical transport by eddy and molecular diffusion, rainout, lightning, particle condensation and diffusion-limited hydrogen escape. Altitude dependent computation is based on incremental 0.5 km grid-steps over 100 km. Within this structure a fixed tropopause is adopted at 11 km. Radiative transfer was computed using a two-stream

approximation using Rayleigh and Mie scattering for gaseous and particulate species, respectively. Photolysis rates were diurnally averaged based on a 50° solar zenith angle. Model integration was performed using a variable time-step reverse-Euler method, which relaxes to Newton's method when large time-steps are large. Only fully converged steady state solutions were analyzed.

The present model incorporates updated SO₂-isotopologue absorption cross sections (33). The previous cross-sections (35) used by Claire *et al.* (7) have been questioned by numerous authors (7, 34), and predict $\Delta^{33}\text{S}$ with the opposite sign to that expected from empirical observations (7). Incorporation of the new cross-sections (33) reverses the $\Delta^{33}\text{S}$ predictions (Figures 4–5), producing $\Delta^{33}\text{S}$ with signs that align with that recorded in the geological record. Importantly for this contribution, Endo *et al.* (33) measured the ³⁶SO₂ isotopologue, allowing $\Delta^{36}\text{S}/\Delta^{33}\text{S}$ to be traced through an atmospheric reaction network for the first time (Figures 4–5). To validate the numerical self-consistency of our isotopic model, we ran the same simulations presented in Figure 4B, but included only mass-dependent fractionation factors. This test scenario (Figure S4) consistently produced $\Delta^{36}\text{S}/\Delta^{33}\text{S}$ slopes near -7.0 as predicted by the theory of mass-conservation (28; Figure S4). Additional validation and more extensive interrogation of the model, and its atmospheric implications, remains beyond the scope of this study and is reserved for a sister manuscript. Here we simply wished to examine the utility of the $\Delta^{36}\text{S}/\Delta^{33}\text{S}$ parameter.

Although there is evidence for the persistence of a Mesoarchean organic haze (10, 20, 78), and the subject of our study is to examine the hypothesized development of periodic Neoproterozoic haze(s) (8, 9), the apparent longevity of $\Delta^{36}\text{S}/\Delta^{33}\text{S} = -0.9$ (64) argues that a clear-skies atmospheric configuration was a more appropriate background state. Accordingly we adopted a haze free standpoint for our standard atmosphere (Figures 4A, 5C) for our modeling efforts, approximating the background atmospheric state following the advent of photosynthesis, yet prior to the GOE. Here, the atmosphere was computed using 2.5 Ga solar flux (79) with a volcanic sulfur flux of 3.85×10^9 molecules cm⁻² s⁻¹ (1 Tmol yr⁻¹) at an H₂S:SO₂ ratio of 1:10 and a volcanic H₂ flux of 1×10^{10} molecules cm⁻² s⁻¹ (3 Tmol yr⁻¹). The volcanic inputs were log-normally distributed vertically throughout the troposphere. Carbon dioxide concentrations were fixed at 1 % irrespective of height, and N₂ provided a balance atmospheric pressure of 1 bar. Further boundary conditions include fixed ground-level mixing ratios of CH₄ (100 ppm) and O₂ (10 ppb). To maintain these mixing ratios in steady state with all other processes, the model computed fluxes of CH₄ (3.6×10^{11} molecules cm⁻² s⁻¹) and O₂ (6.2×10^{11} molecules cm⁻² s⁻¹) that are broadly consistent with predictions of post-oxygenic

photosynthetic Archean biospheric (3, 21, 42). A reducing atmosphere is maintained by elevating volcanic H₂ and H₂S fluxes slightly enhanced from their contemporary level (Case 'V2' of ref. 21) and by a CH₄:O₂ flux ratio > 1:2 (10)

As highlighted in the accompanying manuscript, our hazy simulations do not produce $\Delta^{36}\text{S}/\Delta^{33}\text{S}$ slopes of -1.5 (Figure 5), and the standard model atmosphere fails to reproduce $\Delta^{36}\text{S}/\Delta^{33}\text{S}$ of -0.9 (Figure 4A). The absolute source of this data–model mismatch is unknown; however, it reflects some combination of (i) the uncertainties associated with the prescribed isotopic fractionation factors and/or (ii) the background chemical composition of the Archean atmosphere. Another complication with hazy simulations involves aspects of the numerical computation schemes. While the internal mechanics of clear-skies simulations are well constructed and behaved, the same cannot be said regarding the preliminary simulations presented herein. These model convergence issues decrease our ability to make confident predictions across the entire suite of runs shown in Figure 5. These convergence concerns arise from poor coupling between the chemical, radiative, particle-formation and particle-distribution modules and are compounded by the assumed invariant atmospheric temperature profile. Very recently, major strides have been made in coupling this 1D-photochemical model with a radiative-convective climate model specifically for haze atmospheres, which rectifies many of the aforementioned problems (63). Incorporation of these changes into the isotopic scheme is substantial, and beyond the scope of the present contribution whose aim was more simply to test the utility of the $\Delta^{36}\text{S}/\Delta^{33}\text{S}$ parameter as a proxy for atmospheric chemical composition. Incorporation of these changes will be necessary for future accurate predictive computations of the magnitudes of minor S-isotope effects in hazy atmosphere. While our detailed numerical predictions will certainly be updated, we have satisfied our aim and demonstrated that the altered UV transparency and exit channel importance underneath an organic haze can result in distinct changes in $\Delta^{36}\text{S}/\Delta^{33}\text{S}$, thereby demonstrating the feasibility of the overall hypothesis.

SUPPLEMENTARY FIGURES:

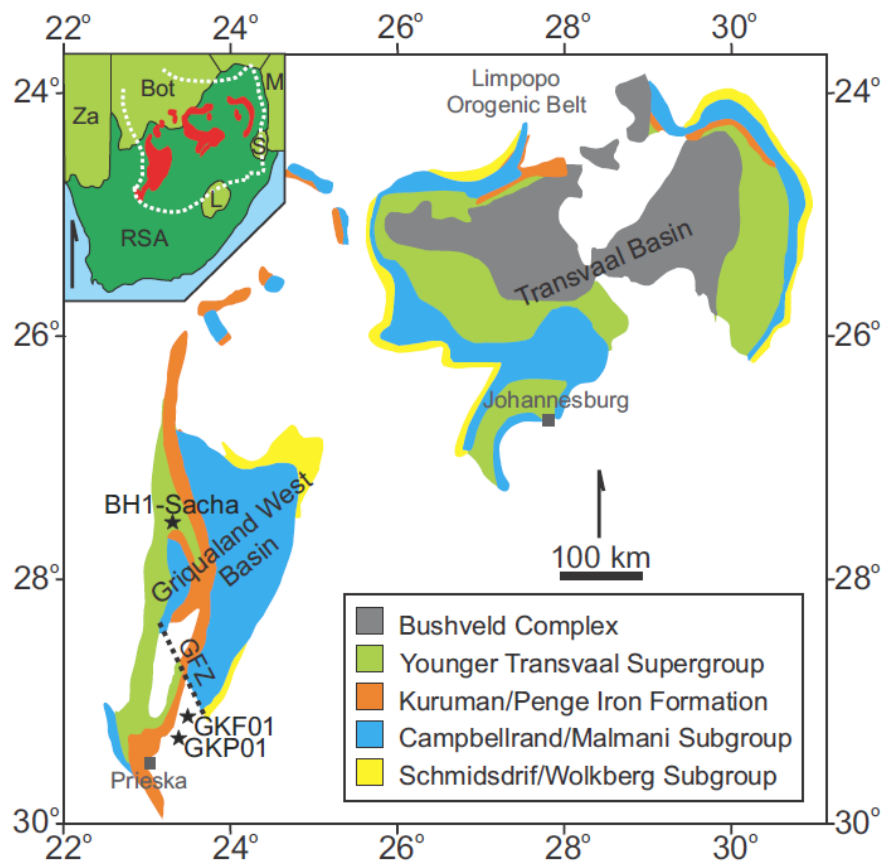


Figure S1: Geological map of the Transvaal Supergroup preserved on the Kaapvaal Craton with a geographical insert, modified from (53) and (51). The position of cores where $\Delta^{36}\text{S}/\Delta^{33}\text{S}-\delta^{13}\text{C}$ covariation has been previously reported (core GKF01, 9; core BH1-Sacha, 8) are indicated by labeled stars. Additionally the extra Agouron core (GKP01) that we discuss below in terms of chronological constraints is also given. The shallow-water Ghaap plateau facies are separated from their deep-water equivalents by the fault at Griquatown (GFZ; 37, 53) hence the different stratigraphic nomenclature between Zerkle *et al.* (9) and Izon *et al.* (8)

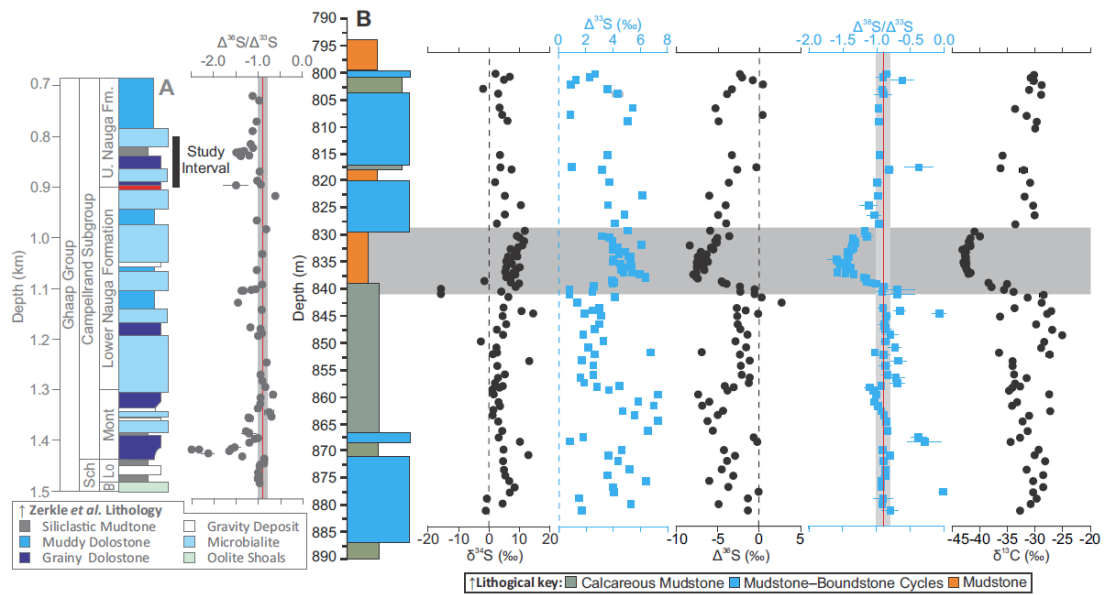


Figure S2: The stratigraphic distribution of the pre-existing (9) and the new S- and C-isotope data ($\delta^{34}\text{S}$, $\Delta^{33}\text{S}$, $\Delta^{36}\text{S}$, $\Delta^{36}\text{S}/\Delta^{33}\text{S}$ and $\delta^{13}\text{C}$). The horizontal grey band illustrates the C-S anomaly, whereas the vertical red lines and their grey envelopes depict the Neoproterozoic reference array and its associated uncertainty (8). Analytical uncertainties are generally encompassed within the data point, whereas uncertainty on the $\Delta^{36}\text{S}/\Delta^{33}\text{S}$ ratio is computed from the larger of the internal or external uncertainties for $\Delta^{36}\text{S}$ and $\Delta^{33}\text{S}$. Note the C-S anomaly pre-dates the lithological change (see also Figure S3).



Figure S3: Initial core photographs corresponding to the onset of the C-S anomaly. The cores young up the page, as signaled by the bold yellow arrow and initial core markings. The older (deeper) core tray (A) is joined to the younger (shallower) tray B by the bold black arrows. The onset of the C-S anomaly (in both $\Delta^{36}\text{S}/\Delta^{33}\text{S}$ and $\delta^{13}\text{C}$) is seen by 840 meters core depth (annotated), whereas the change in lithology (from calcareous mudstone to mudstone) occurs at least 1 m up-core, in younger rocks. Thin red arrows highlight this non-trivial stratigraphic difference. Core photographs and detailed lithological logs of cores GKF01 and GKP01 are available via the Agouron-Griqualand Paleoproterozoic drilling project online database (<http://general.uj.ac.za/agouron/index.aspx>). These photos feature overlap (core markings and vertical blue boxes), and hence repetition of strata, to ensure the entire core was imaged.

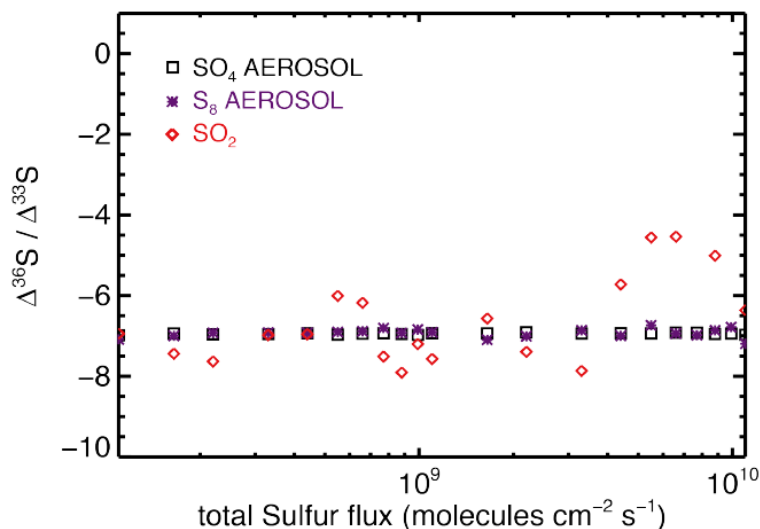


Figure S4: Model validation of the updated photochemical model presented herein. Here multiple simulations have been run with variable atmospheric sulfur loading, with only mass-dependent fractionation factors included. Integrated over the whole atmospheric reaction pathway, the average $\Delta^{36}\text{S}/\Delta^{33}\text{S}$ carried by sulfur (SO_4) aerosols, octasulfur (S_8) aerosols and sulfur dioxide (SO_2) are given by black squares, purple crosses and red diamonds respectively.

CAPTIONS FOR THE APPENDED ELECTRONIC DATASETS:

Table S1 | Tabulated quadruple S-isotope ($\delta^{33}\text{S}$, $\delta^{34}\text{S}$, $\delta^{36}\text{S}$, $\Delta^{33}\text{S}$ and $\Delta^{36}\text{S}$) data in per mille (‰) variations from the V-CDT standard. Internal measurements uncertainties are given at the 1 standard deviation level (σ), whereas the external reproducibility is calculated from replicate Ag_2S fluorinations and are deemed to be 0.02, 0.008 and 0.20 ‰ for $\delta^{34}\text{S}$, $\Delta^{33}\text{S}$, and $\Delta^{36}\text{S}$ respectively. Propagated uncertainties on the $\Delta^{36}\text{S}/\Delta^{33}\text{S}$ ratios are conservatively calculated according to Izon *et al.* (8) using the larger of the internal or the external uncertainties.

Table S2 | Tabulated organic carbon isotope ($\delta^{13}\text{C}_{\text{Org}}$, ‰) and total organic carbon data (TOC). Samples were prepared at the University of St. Andrews and analyzed at JPL Astrobiogeochemistry Laboratory (abcLab) over four analytical sessions. Samples were often run in duplicate and each set of data is shown. Where available the average and standard deviation are calculated for each sample and used in figures within the manuscript. Where duplicates are not available we conservatively apply the average uncertainty calculated from the replicates and note that these do not alter our conclusions.

Table S3 | Tabulated Fe-speciation data determined at the University of St Andrews, with Fe_{Carb} , Fe_{Ox} and Fe_{Mag} determined by sequential extraction (65) and Fe_{AVS} and Fe_{CRS} determined by CrCl_2 distillation; (70). Highly reactive iron (Fe_{HR}) is that reactive towards sulfide on geological timescales and is the sum of Fe_{Carb} , Fe_{Ox} , Fe_{Mag} , Fe_{AVS} and Fe_{CRS} ; whereas, Fe_{Py} is sulfurized fraction of Fe representing the total of Fe_{AVS} and Fe_{CRS} (65).